Astronomy & Astrophysics manuscript no. cores_and_outflows
2016/11/29
©ESO 2016

Thermal Feedback in the high-mass star and cluster forming region W51: Massive Protostars like their food well-done

Adam Ginsburg[1,2], Ciriaco Goddi[3,4], Roberto Galván-Madrid[5], James E. Dale*, John Bally[7], Rowan Smith*, Jeremy Darling[7], J. M. Diederik Kruijssen*, Erik Rosolowsky *, Robert Loughnane[5], Leonardo Testi [1,*,*], Nate Bastian *, Jaime E. Pineda *, Elisabeth Mills *

[1] *European Southern Observatory, Karl-Schwarzschild-Straße 2, D-85748 Garching bei München, Germany*
e-mail: Adam.Ginsburg@eso.org
[2] *National Radio Astronomy Observatory, Socorro, NM 87801 USA*
[*] *Max-Planck-Institut für extraterrestrische Physik, Giessenbachstrasse 1, 85748 Garching, Germany*
[*] *INAF-Osservatorio Astrofisico di Arcetri, Largo E. Fermi 5, I-50125, Florence, Italy*
[*] *Excellence Cluster Universe, Boltzman str. 2, D-85748 Garching bei München, Germany*
[3] *Department of Astrophysics/IMAPP, Radboud University Nijmegen, PO Box 9010, 6500 GL Nijmegen, the Netherlands*
[4] *ALLEGRO/Leiden Observatory, Leiden University, PO Box 9513, 2300 RA Leiden, the Netherlands*
[5] *Instituto de Radioastronomía y Astrofísica, UNAM, A.P. 3-72, Xangari, Morelia, 58089, Mexico*
[*] *Centre for Astrophysics Research, University of Hertfordshire, College Lane, Hatfield, AL10 9AB, UK*
[7] *CASA, University of Colorado, 389-UCB, Boulder, CO 80309*
[*] *Jodrell Bank Centre for Astrophysics, School of Physics and Astronomy, University of Manchester, Oxford Road, Manchester M13 9PL, UK*
[*] *Astronomisches Rechen-Institut, Zentrum für Astronomie der Universität Heidelberg, Mönchhofstraße 12-14, 69120 Heidelberg, Germany*
[*] *Dept. of Physics, University of Alberta, Edmonton, Alberta, Canada*
[*] *Astrophysics Research Institute, Liverpool John Moores University, 146 Brownlow Hill, Liverpool L3 5RF, UK*
[*] *University of California, San Diego TODO finish this*

2016/11/29

ABSTRACT

We present ALMA observations of a 3×1.5 pc area in the W51 high-mass star-forming complex. We identify dust continuum sources and measure the gas and dust temperature through both rotational diagram modeling of CH_3OH and through brightness-temperature-based limits. The observed region contains three high-mass YSOs that appear to be at the earliest stages of their formation, with no signs of ionizing radiation from their central sources. The new data reveal high gas and dust temperatures ($T > 100$ K) extending out to about 5000 AU from each of these sources, indicating that the forming MYSOs are able to heat a large volume of gas in which fragmentation is suppressed. No distinct fragments are observed within this heated zone, though 75 sources representing either prestellar cores or some stage of protostars are detected in the observed field. During the process of forming, these high-mass stars heat a large volume (and correspondingly large mass) of gas, preventing it from fragmenting, and therefore keep a large reservoir available to feed from. By contrast, more mature massive stars that illuminate compact H II regions have little effect on ther surrounding dense gas, hinting that these sources have completed most or all of their accretion. These warm cores are presently stable against Jeans fragmentation, but at their current density and lower temperature, they would not have been, so they must have been assembled from a larger volume of gas.

1. Introduction

High-mass stars are the drivers of galaxy evolution, cycling enriched materials into the interstellar medium (ISM) and illuminating it. During their formation process, however, these stars are nearly undetectable because of their rarity and their opaque surroundings. We therefore know relatively little about how massive stars acquire their mass and what their immedate surroundings look like at this early time.

Assuming the stellar initial mass function (IMF) is a universal (or nearly univeral) distribution (Bastian et al. 2010), massive stars O-stars (with $M > 50 M_\odot$) almost always form in a clustered fashion (in proto-clusters or proto-associations ??Parker & Goodwin 2007). Their presence, and the strong feedback they produce, may directly influence how the IMF around them is formed. If feedback from these stars is relevant while most of the mass surrounding them is still in gas (not yet in stars), the mass function in such clusters cannot be determined by ISM properties alone.

Models of high-mass star formation universally have difficulty collapsing enough material to a stellar radius to form very massive stars. Generally, these models produce a high-mass star with enough luminosity to halt further *spherical* accretion at a very early stage, with $M_* \sim 10 - 20 M_\odot$. Radiation pressure provides a fundamental limit on how much mass can be accreted, but geometric effects can circumvent this limit and allow further accretion (Yorke & Sonnhalter 2002; Krumholz et al. 2005, 2009; Krumholz & Matzner 2009; Kuiper & Yorke 2012, 2013; Rosen et al. 2016). Additionally, fragmentation-induced starvation can limit the

amount of mass available to the most massive star, instead breaking up massive cores into many lower-mass fragments (Peters et al. 2010b). These simulations still have limited physics and can only produce stars up to $M \sim 80\ M_\odot$ even in the current best cases (Kuiper et al. 2015, 2016). The question of how massive stars acquire their mass, and especially whether they ever form Keplerian disks, remains open (Beltrán & de Wit 2016).

Nature is clearly capable of producing massive stars and some that are much larger than those produced in simulations. For example, within the LMC, stars up to $M \sim 300\ M_\odot$ have been spectroscopically identified (Crowther et al. 2016), so we know it is possible to form these. Within our own Galaxy, UV and optical characterization of these stars is not possible, but some infrared lines are indicators of such stars. Barbosa et al. (2008) identified an O3 and an O4 star ($M \gtrsim 50\ M_\odot$) within the W51 IRS2 region, demonstrating that this region has at some time been capable of forming such stars.

The W51 cloud contains two protocluster regions, IRS2 and e1/e2, which each contain $M \gtrsim 10^4\ M_\odot$ of gas and have far-infrared luminosities that indicate the presence of formed or forming massive stars (Harvey et al. 1986; Sievers et al. 1991; Ginsburg et al. 2012, 2016a). Previous millimeter and centimeter observations have revealed the gas that is forming new stars and indicated that the new stars are likely to be massive (Zhang & Ho 1997; Eisner et al. 2002; Zapata et al. 2009; Tang et al. 2009; Zapata et al. 2010; Shi et al. 2010a,b; Koch et al. 2010, 2012a,b; Tang et al. 2012; Goddi et al. 2016). The W51 protoclusters, while distant (5.4 kpc; Sato et al. 2010), therefore provide a powerful laboratory for studying high-mass star formation in an environment where massive star feedback is already evident, but formation is still ongoing.

This combination of feedback and ongoing formation is essential for testing components of high mass star formation theory that are relatively inaccessible to simulations. Krumholz (2006) suggests that accretion heating during the formation of high-mass stars can heat massive cores to $\gtrsim 100$ K and therefore suppress fragmentation into smaller stars, which would be expected for cold cores. While simulations have verified the conclusion that early-stage accretion heating can control the mass scale within low-mass star forming regions (Krumholz et al. 2007; Offner et al. 2011; Bate 2012; Bate et al. 2014), there have been neither theoretical nor observational tests of this model for high-mass stars.

The major sectioning/subsectioning breakdown is awkward. We present an observational study of the high-mass star-forming region W51. In Section 2, we describe the observations and data reduction process. Section 3 describes the analysis, including source identification (§3.1), spatial distribution (§C.1), and photometry (§C.2). We then examine the source temperatures (§C.3) in order to determine their nature (§C.4). We examine the most massive cores in Sections 3.1.1 and 3.1.2 and then compute their radial mass profiles in 3.5. Section 3.2 describes the mass and flux recovered on different spatial scales, Section 3.3 the observed chemical distribution, and Section 3.4 the temperatures inferred from CH_3OH lines (§3.4). Section 3.6 shows that the heating is not coming from H II regions. Section B and its subsections describe outflows Section 4 discusses scales and types of feedback (§4.1), outflows (§4.1.2), accretion and outflows (§4.2), and fragmentation (§4.4). We conclude in Section 5. Additional interesting features in the W51 data not directly relevant to our main topic are discussed in Appendix A.

2. Observations

As part of ALMA Cycle 2 program 2013.1.00308.S, we observed a $\sim 2' \times 1'$ region centered between W51 IRS2 and W51 e1/e2 with a 37-pointing mosaic. Two configurations of the 12m array were used, achieving a resolution of $0.2''$. Additionally, a 12-pointing mosaic was performed using the 7m array, hypothetically probing scales up to $\sim 28''$. The full UV coverage was from ~ 12 to ~ 1500 m. The spectral windows (SPWs) covered are listed in Table 1, and the lines they cover described in Section 2.1.2.

Additionally, we will comment briefly on project 2015.1.01569.S (PI: Goddi), which observed two fields centered on e2e/e8 and north with very long baselines (resolution $0.04''$) and provide additional insights that our $0.2''$ data do not yield alone. Full details of that data set will be released in a future work.

2.1. Data Reduction

Data reduction was performed using CASA. The QA2-produced data products were combined using the standard inverse variance weighting. Two sets of images were produced for different aspects of the analysis, one including the 7m array data and one including only 12m data. Except where otherwise noted, the 12m-only data were used in order to focus on the compact structures.

Full details of the data reduction, including all scripts used, can be found on the project's github repository[1].

2.1.1. Continuum

A continuum image combining all 4 spectral windows was produced using `tclean`. We identified line-rich channels from a spectrum of source e8 and flagged them out prior to imaging. We then phase self-calibrated the data on baselines longer than 100m to increase the dynamic range. The final image was cleaned with 50000 iterations to a threshold of 5 mJy. The lowest noise level in the image, away from bright sources, is ~ 0.2 mJy/beam ($M \sim 0.14\ M_\odot$ at $T = 20$ K using the extrapolation of Ossenkopf & Henning (1994) opacity from Aguirre et al. (2011) with $\beta = 1.75$), but near the bright sources e2 and IRS2, the noise reached as high as ~ 2 mJy/beam. Deeper cleaning was attempted, but lead to instabilities. The combined image has a central frequency of about 226.6 GHz assuming a flat spectrum source; a steep-spectrum source, with $\alpha = 4$, would have a central frequency closer to 227 GHz, a difference that is negligible for all further analysis.

2.1.2. Lines

We produced spectral image cubes of the lines listed in Tables 2, 3, 4, and 5. For kinematic and moment analysis, the median value over the spectral range [25,30],[80,95] km s^{-1} was used to estimate and subtract the local continuum.

[1] https://github.com/keflavich/W51_ALMA_2013.1.00308.S

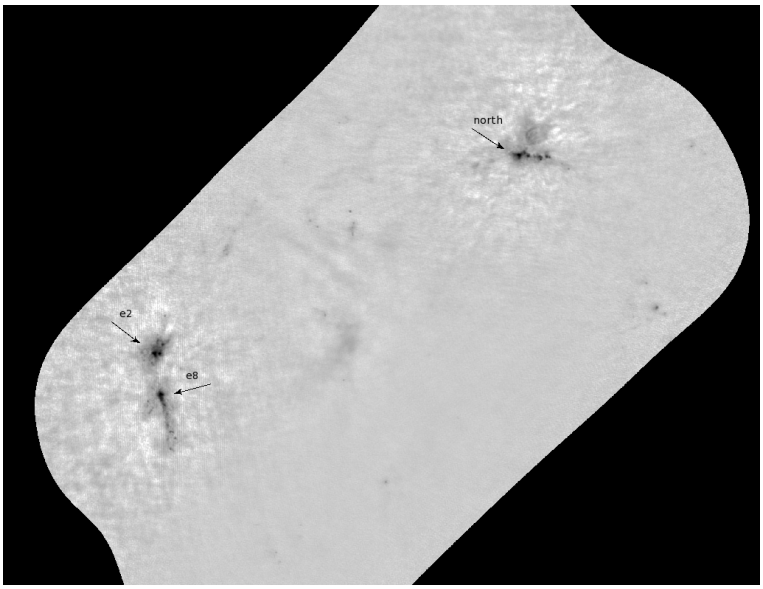

Fig. 1. An overview of the W51A region as seen by ALMA. The grayscale shows a 1.3mm ALMA image. This is a placeholder

Table 1. Spectral Setup

SpwID	Minimum Frequency GHz	Maximum Frequency GHz	Channel Width kHz
0	218.11930228	218.619301	-122.07
1	218.36288652	220.355073	-488.281
2	230.376575	232.36876148	488.281
3	232.981075	234.97326148	488.281

Table 2. Spectral Lines in SPW 0

Line Name	Frequency GHz
H_2CO $3_{0,3} - 2_{0,2}$	218.22219
H_2CO $3_{2,2} - 2_{2,1}$	218.47564
CH_3OH $4_{2,2} - 3_{1,2}$	218.44005
CH_3OCHO $17_{3,14} - 16_{3,13}$E	218.28083
CH_3OCHO $17_{3,14} - 16_{3,13}$A	218.29787
CH_3CH_2CN $24_{3,21} - 23_{3,20}$	218.39002
Acetone $8_{7,1} - 7_{4,4}$AE	218.24017
$O^{13}CS$ 18-17	218.19898
CH_3OCH_3 $23_{3,21} - 23_{2,22}$AA	218.49441
CH_3OCH_3 $23_{3,21} - 23_{2,22}$EE	218.49192
CH_3NCO $25_{1,24} - 24_{1,23}$	218.5418
CH_3SH $23_2 - 23_1$	218.18612

3. Results & Analysis

3.1. Source Identification

We used the `dendrogram` method described by Rosolowsky et al. (2008) and implemented in `astrodendro` to identify sources. We used a minimum value of 1 mJy/beam ($\sim 5\sigma$) and a minimum $\Delta = 0.4$ mJy/beam ($\sim 2\sigma$) with minimum 10 pixels (each pixel is $0.05''$). This cataloging yielded over 8000 candidate sources, of which the majority are noise or artifacts around the brightest sources. To filter out these bad sources, we created a noise map taking the local RMS of the `tclean`-produced residual map over a $\sigma = 30$ pixel ($1.5''$) gaussian. We then removed all sources with peak S/N < 8, mean S/N per pixel < 5, and minimum S/N per pixel < 1. We also only included the smallest sources in the dendrogram, the "leaves". These parameters were tuned by checking against "real" sources identified by eye and selected using `ds9`: most real sources are recovered and few spurious sources (< 10) are included. The resulting catalog includes 113 sources.

The 'by-eye' core extraction approach, in which we placed ds9 regions on all sources that look 'real', produced a more reliable but less complete (and less quantifiable) catalog containing 75 sources. This catalog is more useful in the regions around the bright sources e2 and north, since these regions are affected by substantial uncleaned PSF sidelobe artifacts. In particular, the dendrogram catalog includes a number of sources around e2/e8 that, by eye, appear to be parts of continuous extended emission rather than local peaks; "streaking" artifacts in the reduced data result in

Table 3. Spectral Lines in SPW 1

Line Name	Frequency GHz
H_2CO $3_{2,1} - 2_{2,0}$	218.76007
HC_3N 24-23	218.32471
HC_3Nv_7=1 24-23a	219.17358
HC_3Nv_7=1 24-23a	218.86063
HC_3Nv_7=2 24-23	219.67465
OCS 18-17	218.90336
SO $6_5 - 5_4$	219.94944
HNCO $10_{1,10} - 9_{1,9}$	218.98102
HNCO $10_{2,8} - 9_{2,7}$	219.73719
HNCO $10_{0,10} - 9_{0,9}$	219.79828
HNCO $10_{5,5} - 9_{5,4}$	219.39241
HNCO $10_{4,6} - 9_{4,5}$	219.54708
HNCO $10_{3,8} - 9_{3,7}$	219.65677
CH_3OH $8_{0,8} - 7_{1,6}$	220.07849
CH_3OH $25_{3,22} - 24_{4,20}$	219.98399
CH_3OH $23_{5,19} - 22_{6,17}$	219.99394
$C^{18}O$ 2-1	219.56036
H_2CCO 11-10	220.17742
HCOOH $4_{3,1} - 5_{2,4}$	219.09858
CH_3OCHO $17_{4,13} - 16_{4,12}$A	220.19027
CH_3CH_2CN $24_{2,22} - 23_{2,21}$	219.50559
Acetone $21_{1,20} - 20_{2,19}$AE	219.21993
Acetone $21_{1,20} - 20_{1,19}$EE	219.24214
Acetone $12_{9,4} - 11_{8,3}$EE	218.63385
$H_2{}^{13}CO$ $3_{1,2} - 2_{1,1}$	219.90849
SO_2 $22_{7,15} - 23_{6,18}$	219.27594
SO_2 $v_2 = 1$ $20_{2,18} - 19_{3,17}$	218.99583
SO_2 $v_2 = 1$ $22_{2,20} - 22_{1,21}$	219.46555
SO_2 $v_2 = 1$ $16_{3,13} - 16_{2,14}$	220.16524

Table 4. Spectral Lines in SPW 2

Line Name	Frequency GHz
^{12}CO $2 - 1$	230.538
OCS 19-18	231.06099
HNCO $28_{1,28} - 29_{0,29}$	231.873255
CH_3OH $10_{2,9} - 9_{3,6}$	231.28115
^{13}CS 5-4	231.22069
NH_2CHO $11_{2,10} - 10_{2,9}$	232.27363
H30α	231.90093
CH_3OCHO $12_{4,9} - 11_{3,8}$E	231.01908
CH_3CH_2OH $5_{5,0} - 5_{4,1}$	231.02517
CH_3OCH_3 $13_{0,13} - 12_{1,12}$AA	231.98772
N_2D+ 3-2	231.32183
g-CH_3CH_2OH $13_{2,11} - 12_{2,10}$	230.67255
g-CH_3CH_2OH $6_{5,1} - 5_{4,1}$	230.79351
g-CH_3CH_2OH $16_{5,11} - 16_{4,12}$	230.95379
g-CH_3CH_2OH $14_{0,14} - 13_{1,13}$	230.99138
SO_2 $v_2 = 1$ $6_{4,2} - 7_{3,5}$	232.21031
CH_3SH $16_2 - 16_1$	231.75891
CH_3SH $7_3 - 8_2$	230.64608

their identification despite our threshold criteria. The dendrogram extraction also identified sources within the IRS 2 H II region that are not dust sources. Dendrogram extraction missed a few clear sources in the low-noise regions away from W51 Main and IRS 2 because the identification criteria were too conservative.

When extracting properties of the 'by-eye' sources, we used variable sized circular apertures, where the apertures were selected to include all of the detectable symmetric emission around a central peak up to a maximum radius $r \sim 0.6''$. This approach is necessary, as some of the sources

Table 5. Spectral Lines in SPW 3

Line Name	Frequency GHz
CH_3OH $4_{2,3} - 5_{1,4}$	234.68345
CH_3OH $5_{-4,2} - 6_{-4,3}$	234.69847
CH_3OH $18_{3,15} - 17_{4,14}$	233.79575
$^{13}CH_3OH$ $5_{1,5} - 4_{1,4}$	234.01158
PN $5 - 4$	234.93569
NH_2CHO $11_{5,6} - 10_{5,5}$	233.59451
Acetone $12_{11,2} - 11_{10,1}$AE	234.86136
SO_2 $16_{6,10} - 17_{5,13}$	234.42159
CH_3NCO $27_{2,26} - 26_{2,25}$	234.08812
CH_3SH $15_2 - 15_1$	234.19145

are not centrally peaked and are therefore likely to be spatially resolved starless cores.

Further information about and general discussion of the continuum sources is in Appendix C. For the rest of this section, we focus on only the few brightest sources.

3.1.1. W51e2e mass and temperature estimates from continuum

In a $0.21'' \times 0.19''$ beam (1100×1000 au), the peak flux density toward W51 e2e is 0.38 Jy, which corresponds to a brightness temperature $T_B = 225$ K. This is a lower limit to the surface brightness of the millimeter core, since an optical depth $\tau < 1$ or a filling factor of the emission $ff < 1$ would both imply higher intrinsic temperatures. The implied luminosity, assuming blackbody emission from a spherical beam-filling source, is $L = 4\pi r^2 \sigma_{sb} T^4 = 2.3 \times 10^4 L_\odot$. Since any systematic uncertainties imply a higher temperature, this estimate is a lower limit on the source luminosity. Such a luminosity corresponds to a B0.5V, 15 $M_\odot$ star with effective temperature 4×10^4 K (Pecaut & Mamajek 2013, see Section 4.3 for further discussion of stellar types).

If we assume that the dust is optically thick throughout our beam, and assume an opacity constant $\kappa(226\mathrm{GHz}) = 120$ g cm^{-2}, the minimum mass per beam to achieve $\tau \geq 1$ is $M = 18$ $M_\odot$ beam^{-1}. This mass is not a strict limit in either direction: if the dust is indeed optically thick, there may be substantial hidden or undetected gas, while if the filling factor is lower than 1, the dust may be much hotter and therefore optically thin and lower mass. However, simulations and models both predict that the dust will become highly optically thick at radii $r \lesssim 1000$ au (Forgan et al. 2016; Klassen et al. 2016), so it is likely that this measurement provides a lower limit on the total gas mass surrounding the protostar. Therefore, unless the stars are extremely efficient at removing material or the gas fragments significantly on < 1000 AU scales, the stellar mass is likely to at least double before accretion halts.

For an independent measurement of the temperature that is not limited to the optically thick regions, we use the CH_3OH lines in band, calculating an LTE temperature that is $200 < T < 600$ K out to $r < 2''$ ($r < 10^4$ au; Section 3.4). As noted in Section 3.4, these temperatures may be overestimates when the low-J lines of CH_3OH are optically thick, but for now they are the best measurements we have available. If the dust temperature matches the methanol temperature, it would be optically thin ($\tau \lesssim 1/3$) and the central source dust mass would be only ~ 6 $M_\odot$. However, this latter estimate discounts any substructure at scales $<$ 1000 AU, which we know exists from the 2015.1.01596.S data.

An upper limit on the radio continuum emission from W51e2e is $S_{14.5GHz} < 0.6$ mJy/beam in a FWHM=$0.34''$ beam, or $T_{B,max} < 30$ K (Ginsburg et al. 2016a). Assuming emission from an optically thick H II region with $T_e = 8500$ K (Ginsburg et al. 2015), the upper limit on the emitting radius is $R_{\mathrm{H\,II}} < 110 AU$. Similar limits are obtained from other frequencies in those data. The free-free contribution to the millimeter flux is therefore negligible, and the central source is unlikely to be ionizing. Limits on the stellar properties are further discussed in Section 4.3.

3.1.2. W51 e8 and north mass and temperature from continuum

We repeat the above analysis for e8 and north. They have peak flux densities of 0.35 and 0.44 Jy/beam respectively, corresponding to peak brightness temperatures of 205 and 256 K. The lower limit luminosities of W51 e8 and north in a single beam, assuming the brightest detected beam is optically thick, are 1.6×10^4 and 3.9×10^4 $L_\odot$, respectively.

W51 North has an upper limit similar to that of W51e2e, but somewhat less restrictive because the noise in that region is substantially higher. W51 e8, by contrast with the others, has a clear detection at cm wavelengths. The source e8n, which is offset from the peak mm emission by $0.13''$ (700 AU), has $S_{25GHz} = 4.7$ mJy/beam, corresponding to $T_B = 135$ K, which implies an optically thick H II region size $R = 180$ AU. This could be part of an ionized jet or an ionizing binary companion, but its offset from the central mm source suggests that it is not a simple spherically symmetric HCH II region.

3.2. The mass and light budget on different spatial scales

An evolutionary indicator used for star-forming regions is the amount of mass at a given density; a more evolved (or more efficiently star-forming) region will have more mass at high densities. We cannot measure the dense gas fraction directly, but the amount of flux density recovered by an interferometer provides an approximation.

For the "total" flux density in the region, we use the Bolocam Galactic Plane Survey observations (Aguirre et al. 2011; Ginsburg et al. 2013), which are the closest in frequency single-dish millimeter data available. We assume a

spectral index $\alpha = 3.5$ to convert the BGPS flux density measurements at 271.4 GHz to the mean ALMA frequency of 226.6 GHz. The ALMA data (specifically, the 0.2″ resolution 12m-only data) have a total flux 23.2 Jy above a conservative threshold of 10 mJy/beam in our mosaic; in the same area the BGPS data have a flux of 144 Jy, which scales down to 76.5 Jy. The recovery fraction is 30±3%, where the error bar accounts for a change in $\alpha \pm 0.5$. The threshold of 10 mJy/beam corresponds to a column threshold $N > 1.3 \times 10^{25}$ cm^{-3} for 20 K dust. This threshold also corresponds to an optical depth of $\tau \approx 0.5$, implying that a large fraction of the cloud is either approaching optically thick or is warmer than 20 K. For an unresolved spherical source in the $\sim 0.2''$ beam, this column density corresponds to a volume density $n > 10^{8.1}$ cm^{-3}.

Even more impressive is the amount of the total flux density concentrated into the three 'massive cores', W51 e2e, e8, and north. These three contain 12.3 Jy (within 1″ or 5400 AU apertures) of the total 23.2 Jy in the observed field - more than half of the total ALMA flux density, or 15% of the BGPS flux density. In a Kroupa (2001) IMF, massive stars ($M > 20\ M_\odot$) account for only 0.15% of the mass, so in order for the gas mass distribution to produce a 'normal' stellar distribution, the high-mass-star-producing gas must be much brighter (hotter) than that making low-mass stars, or the gas must be substantially redistributed and fragmented as the region evolves.

3.3. Chemically Distinct Regions

The "hot cores" in W51 (e2, e8, and North) are spatially well-resolved and multi-layered. These cores are detected in lines of many different species spanning areas $\sim 5\times10^3 - 10^4$ AU across.

Surrounding W51e2e, there are relatively sharp-edged uniform-brightness regions in a few spectral lines over the range 51-60 km s^{-1} (Figure 2). Some of these features are elongated in the direction of the outflow, but most have significant extent orthogonal to the outflow, spanning 9500×6600 AU. They are prominent in CH_3OH, OCS, and CH_3OCH_3, weak but present in H_2CO and SO, and absent in HC_3N and HNCO.

Around e8, a similar feature is observed, but in this case CH_3OCH_3 is absent. Toward W51 north, CH_3OH, H_2CO, and SO exhibit the sharp-edged enhancement feature, while the other species do not. The enhancement is from 50-60 km s^{-1}.

By contrast, along the south end of the e8 filament, no such enhanced features are seen; only H_2CO and the lowest transition of CH_3OH are evident.

The relative chemical structures of e2, e8, and IRS2 are similar. The same species are detected in all of the central cores. However, in e2, CH_3OCH_3, CH_3OCHO, CH_3CH_2CN, and Acetone ($[CH_3]_2$ CO) are significantly more extended than in the other sources. g-CH_3CH_2OH is detected in W51 North, but is weak in e8 and almost absent in e2 (Figures 2, 3, 4, 5).

Different chemical groups exhibit different morphologies around e2. Species that are elongated in the NW/SE direction are associated primarily with the outflow (HC_3N, CH_3CH_2CN). Other species are associated primarily with the extended core (CH_3OCHO, CH_3OCH_3, $[CH_3]_2$ CO). Some are only seen in the compact core (H_2CN, HNCO, NH_2CHO, and vibrationally excited HC_3N). Only CH_3OH and OCS are associated with both the extended core and the outflow, but not the greater extended emission. H_2CCO seems to be associated with only the extended core, but not the compact core. Finally, there are the species that trace the broader ISM in addition to the cores and outflows (H_2CO, ^{13}CS, OCS, $C^{18}O$ and SO). Both HCOOH and N_2D+ are weak and associated only with the innermost e2e core.

The presence of these complex species symmetrically distributed at large distances ($r \sim 5000$ AU) from the central sources is an independent indication of the gas heating provided by these sources.

3.4. CH_3OH temperatures & columns in the hot cores

The chemically enhanced regions appear to be associated with regions of elevated gas temperature. We examine this directly by analyzing the excitation of lines for which we have detected multiple transitions with significant energy differences. We do not use H_2CO for this analysis despite its usefulness as a thermometer because it is clearly optically thick (self-absorbed) in all lines in the hot cores.

We produce rotational diagrams for each spatial pixel covering all CH_3OH lines detected at high significance toward at least one position. The detected lines span a range $45 < E_U < 800$ K, allowing robust measurements of the temperature assuming the lines are optically thin, in LTE, and the gas temperature is high enough to excite the lines. These conditions are likely to be satisfied in the e2e, e8, and North cores, except for the optically thin requirement. Luckily, there are some lines in band that have much lower Einstein $A_{i,j}$ values but comparable upper-state energy levels, allowing us to probe higher column densities than would otherwise be possible.

Sample fitted rotational diagrams are displayed in Figure 7. The line intensities are computed from moment maps integrating over the range (51, 60) km s^{-1} in continuum-subtracted spectral cubes, where the continuum was estimated as the median over the ranges (25-35,85-95) km s^{-1}, except for the J=25 lines, which had a continuum estimated from the 10th percentile over the same range to exclude contamination from the SO outflow line wings.

To validate some of the rotational diagram fits, we examined the modeled spectra overlaid on the real (Figure 8). These generally display significant discrepancies, especially at low J where self-absorption is evident. In Figure 8, there is clearly a low-temperature component slightly redshifted from the high-J peak that can be seen as a dip within the line profile. The presence of this unmodeled low-temperature component renders our CH_3OH temperature measurements uncertain. Nevertheless, the general trend exhibited by CH_3OH temperatures matches expectations if there is a central heating source.

Figure 9 shows a comparison between the CH_3OH $10_{2,9} - 9_{3,6}$ line and the 225 GHz continuum. While the brightest regions in CH_3OH mostly have corresponding dust emission, the dust morphology traces the CH_3OH morphology very poorly. This difference suggests that the enhanced brightness is not simply because of higher total column density. We examine the dust-CH_3OH link more quantitatively in Figure 11.

Figure 10 shows the observed brightness profiles of CH_3OH line and dust continuum emission. Figure 11 shows a comparison of the CH_3OH temperature and abundance.

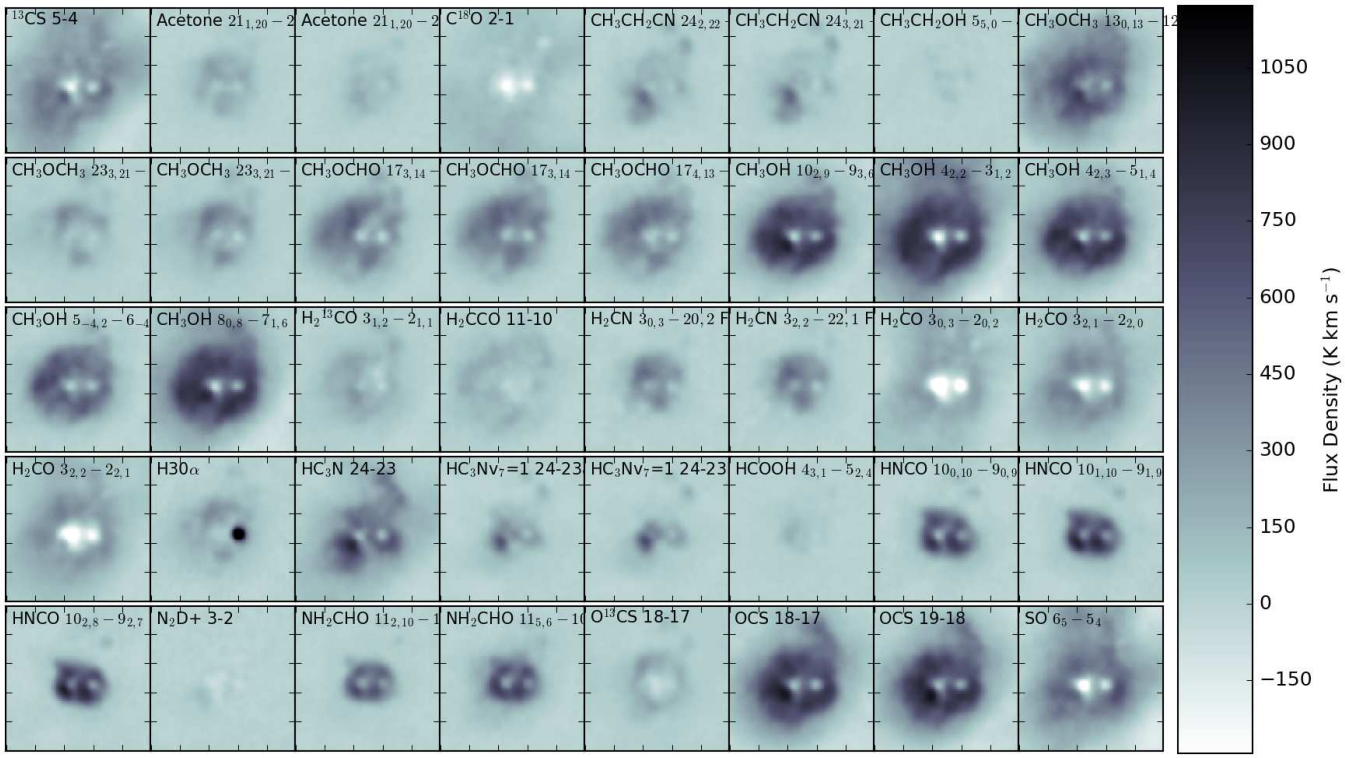

Fig. 2. Moment 0 maps of the e2 region in 40 different lines over the range 51 to 60 km s^{-1} with continuum subtraction using the 30th percentile emission over the ranges 25-40 and 75-90 km s^{-1}. All images are on the same scale, and the negative features show absorption against the continuum. There is a strong 'halo' of emission seen in the CH_3Ox lines and OCS. Extended emission is also clearly seen in SO, ^{13}CS, and H_2CO, though these lines more smoothly blend into their surroundings. HNCO and NH_2CHO have smaller but substantial regions of enhancement with a sharp contrast to their surroundings. HC_3N traces the e2 outflow. The bright H30α emission marks the position of e2w, the hypercompact HII region that dominates the centimeter emission in e2.

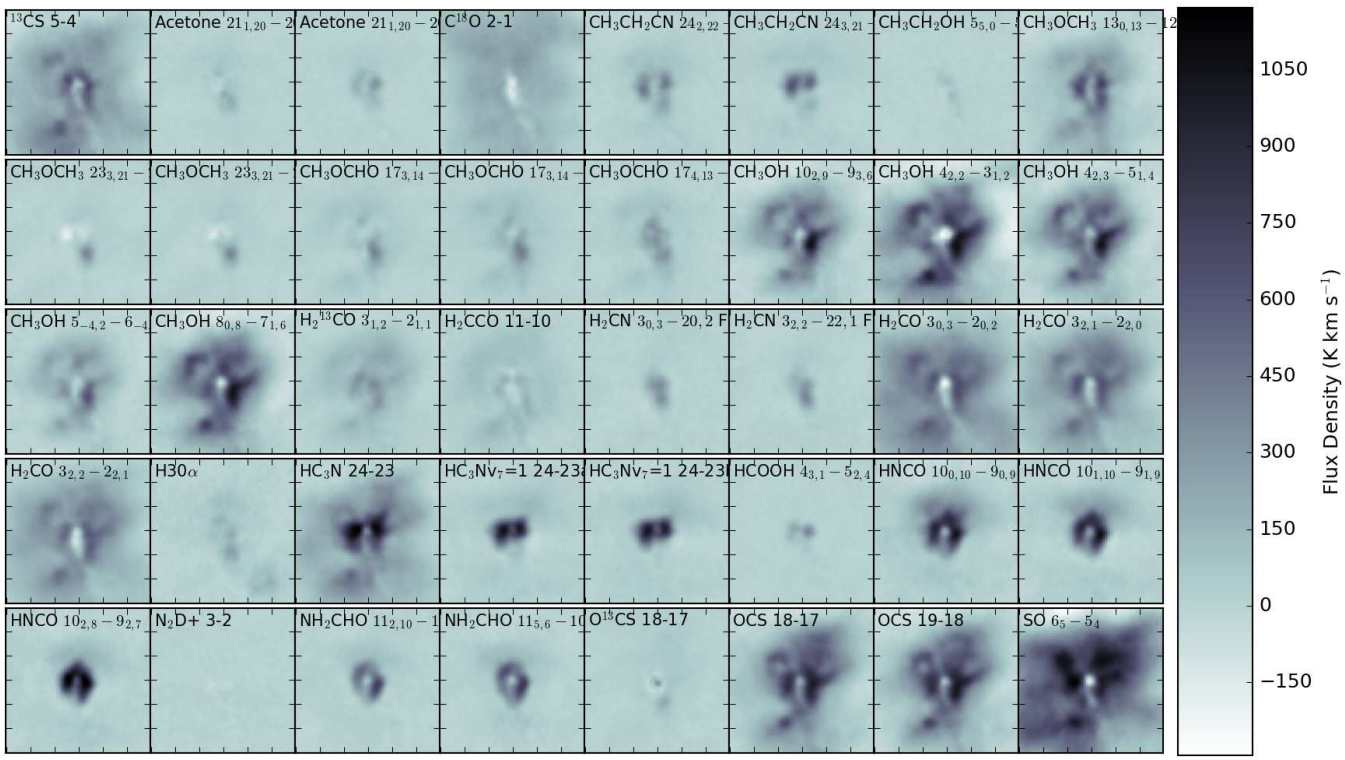

Fig. 3. Moment 0 maps of the e8 region in 40 different lines over the range 52 to 63 km s^{-1} with continuum subtraction using the 30th percentile emission over the ranges 25-40 and 75-90 km s^{-1}. All images are on the same scale, and the negative features show absorption against the continuum. As in e2, there is extended emission in the CH_3OH and OCS lines, but in contrast with e2, the other CH_3Ox lines are more compact. SO is brighter than OCS in e8, whereas the opposite is true in e2.

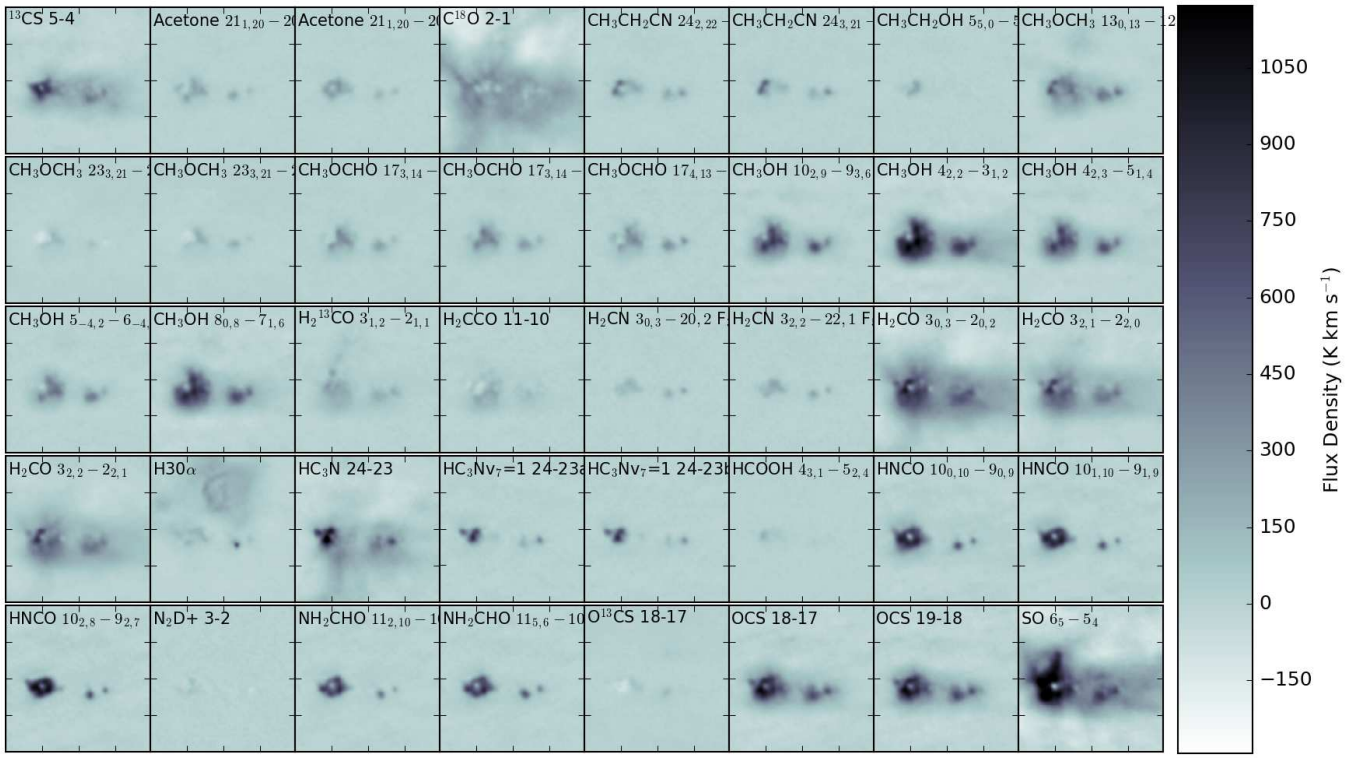

Fig. 4. Moment 0 maps of the W51 IRS2 region in 40 different lines over the range 54 to 64 km s^{-1} with continuum subtraction using the 30th percentile emission over the ranges 25-40 and 75-90 km s^{-1}. All images are on the same scale, and the negative features show absorption against the continuum. Qualitatively, the relative extents of species seem comparable to e8. The H30α point source is W51 d2.

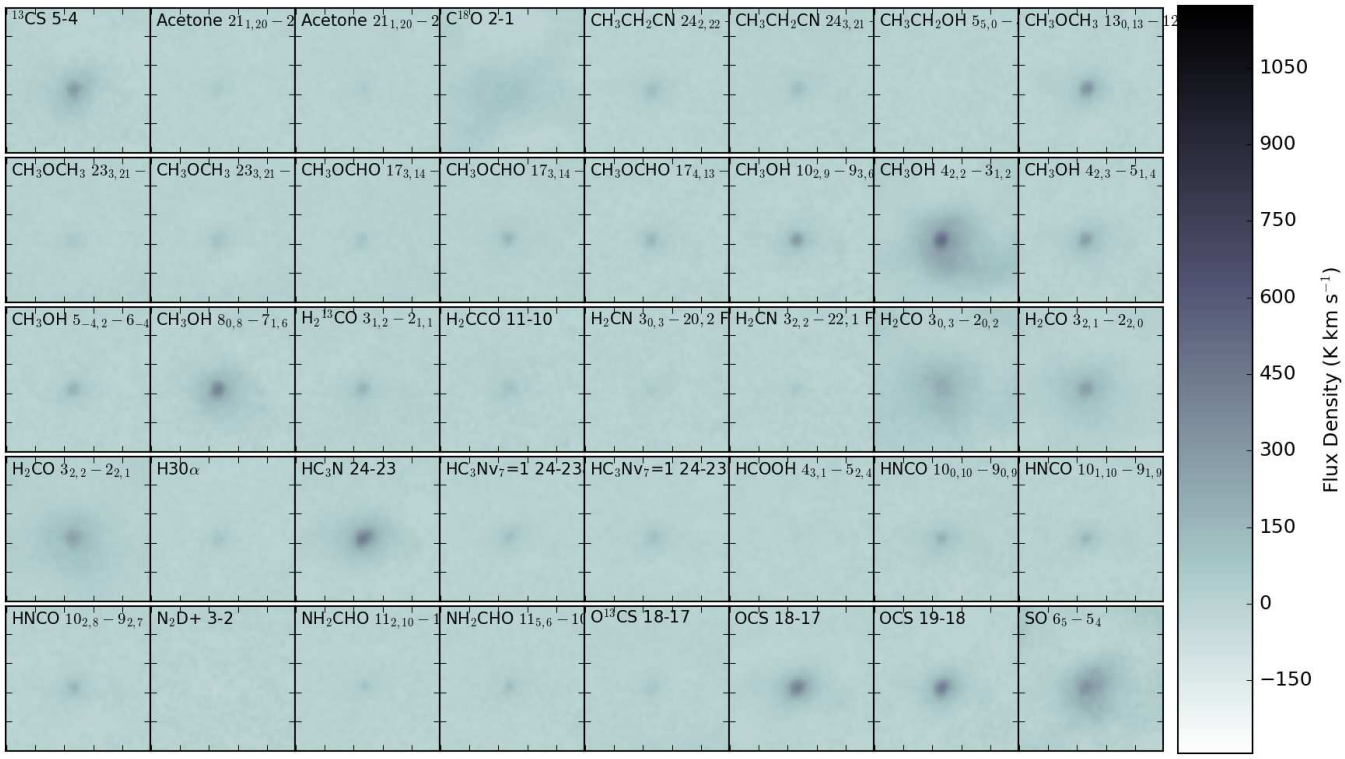

Fig. 5. Moment 0 maps of the ALMAmm14 region in 40 different lines over the range 58 to 67 km s^{-1} with continuum subtraction using the 30th percentile emission over the ranges 25-40 and 75-90 km s^{-1}. All images are on the same scale. ALMAmm14 is one of the brightest sources outside of e2/e8/IRS2, but it is substantially fainter than those regions. Still, it has a noticeably rich chemistry.

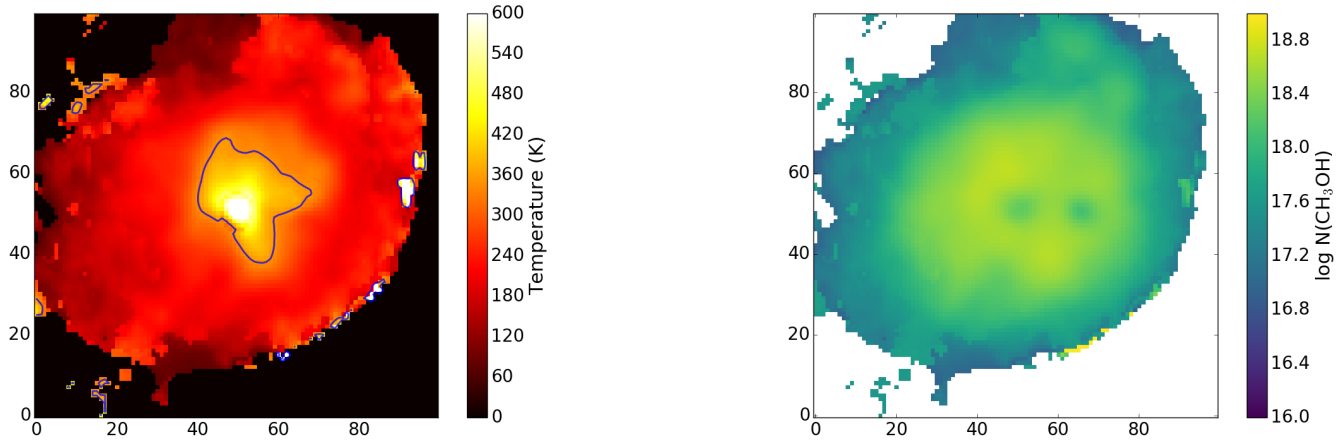

(a) (b)

Fig. 6. Methanol temperature and column density maps around e2. The central regions around the cores appear to have lower column densities because the lines become optically thick and self-absorbed. The contour in the temperature map is at 350 K, where red meat is typically considered "well-done".

The CH_3OH abundance is derived by comparing the rotational diagram (RTD) fitted CH_3OH column density to the dust column density while using the CH_3OH-derived temperature as the assumed dust temperature. The figure shows all pixels within a $3''$ (16200 AU) radius of e2e, with pixels having low column density and high temperature (i.e., pixels with bad fits) and those near e2w (which may be heated by a different source) excluded. We used moment-0 (integrated intensity) maps of the CH_3OH lines to perform these RTD fits, which means we have ignored the line profile entirely and in some cases underestimated the intensity of the optically thick lower-J lines: in the regions of highest column, the column is underestimated and the temperature is overestimated, as can be seen in Figure 8.

A few features illustrate the effects of thermal radiative feedback on the gas. The temperature jump starting inwards of $r \sim 1.5''$ (8100 AU; Figure 11b) is substantial, though the 100-200 K floor at greater radii is likely artificial as the low-J transitions are not consistent with a thermal distribution. There is an abundance enhancement at the inner radii, but it appears to be a radial bump rather than a pure increase. The abundance enhancement is probably real, and is approximately a factor of $\sim 5-10$. The inner abundance dip is caused by two coincident effects: first, the CH_3OH column becomes underestimated because the CH_3OH is *self*-absorbed, and second, the dust becomes optically thick, blocking additional CH_3OH emission, though this latter effect is somewhat self-regulating since it also decreases the dust column (the denominator in the abundance expression).

3.5. Radial mass profiles around the most massive cores

In Figure 12, we show the radial profiles extracted from the three high-mass protostellar cores in W51: W51 North, W51 e2e, and W51 e8. The plot shows the enclosed mass out to $\sim 1''$ (5400 AU). On larger spatial scales, the enclosed mass rises more shallowly, indicating the end of the core.

All three sources show similar radial profiles, containing up to 3000 $M_\odot$ within a compact radius of 5400 AU (0.03 pc). However, the temperature structure within these sources is certainly not homogeneous, and likely a large fraction of the total flux comes from $T \gtrsim 300$ K heated material (Section C.3; Goddi et al. 2016). If the observed dust were all at 600 K, the mass would be $\sim 17\times$ lower, 100 $M_\odot$, which we treat as a strict lower bound as it is unlikely that the dust at more than $r \gtrsim 1000$ AU is so warm. Additionally, it is likely that a substantial mass of cold dust is also present but undetectable because it is hidden by the hotter dust.

3.6. Ionizing vs non-ionizing radiation

The formed and forming protostars are producing a total $\gtrsim 10^7$ $L_\odot$ of far infrared illumination (Ginsburg et al. 2016a). This radiation heats the cloud's molecular gas, affecting the initial conditions of future star formation.

The ionizing radiation in W51 was discussed in detail in Ginsburg et al. (2016a). Ionizing radiation affects much of the cloud volume, but little of the high-density prestellar material: there is no evidence of increased gas temperatures in the vicinity of H II regions. While in Section 3.3 we identify chemically enhanced regions as those where radiative feedback has heated the dust and released ices into the gas phase, no such regions are observed surrounding the compact H II regions.

The chemical maps shown in Section 3.3 show the volumes of gas clearly affected by newly-forming high-luminosity stars. The CH_3OH-enhanced region around W51e2e extends 0.04 pc, or 8500 AU (see Section 3.4). Other locally enhanced species, especially the nitrogenic molecules HNCO and NH_2CHO, occupy a smaller and more asymmetric region around e2e and e2w (Figure 14). These chemically enhanced regions are most prominent around the weakest radio sources or regions with no radio detection; they are most likely heated by direct infrared radiation from these sources.

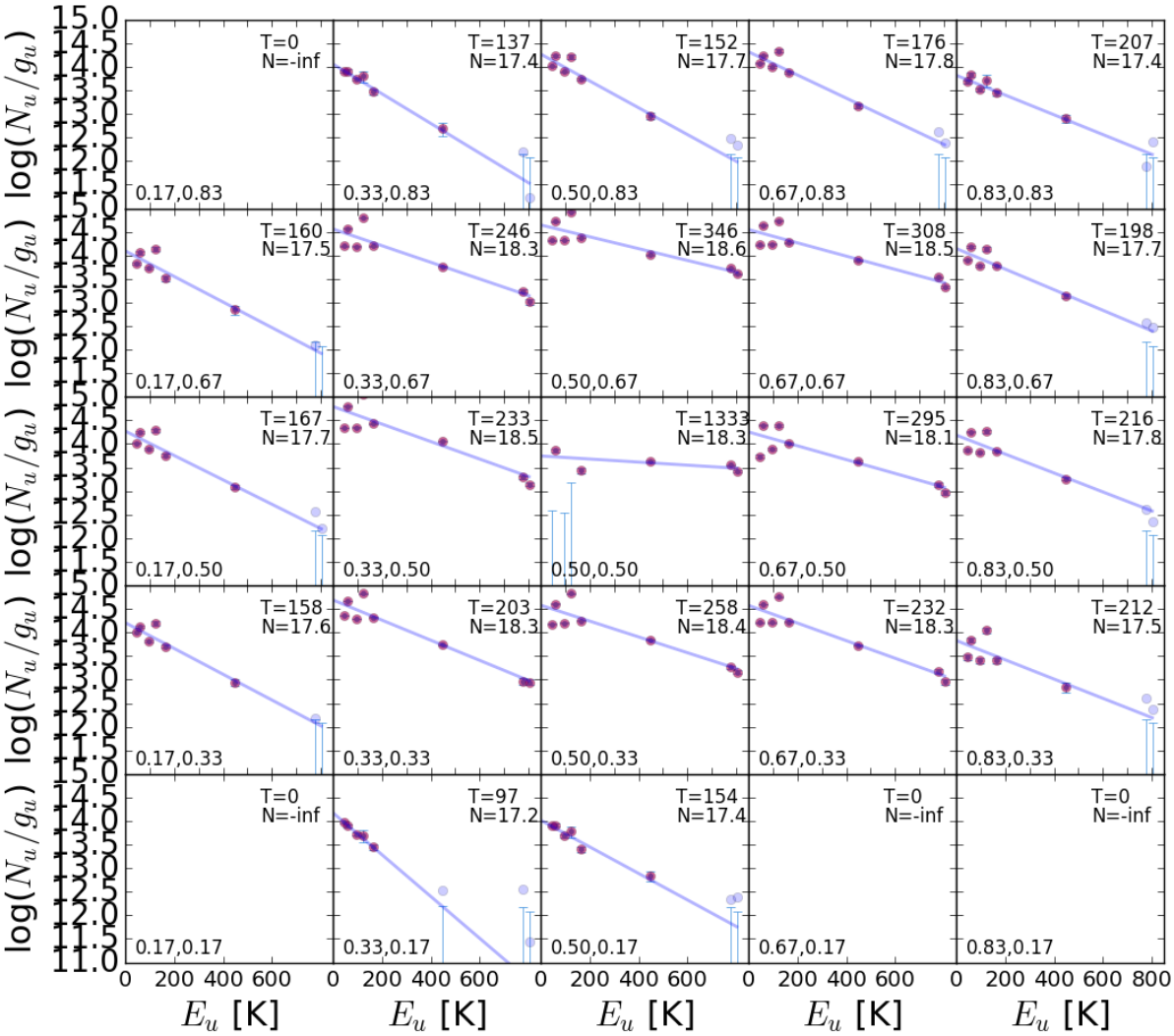

Fig. 7. A sampling of fitted rotation diagrams of the detected CH_3OH transitions. These are meant to provide validation of the temperatures and column densities derived and shown in Figure 6. The lower-left corner shows the position from which the data were extracted in that figure in units of figure fraction. The horizontal black lines show the detection threshold of each of the transitions; points below these lines are ignored when fitting, and instead the threshold itself is used. The fitted temperature and column are shown in the top right of each plot.

3.7. Outflows

While many outflows were detected, we defer their discussion to Appendix B, as the details of these flows is not relevant to the main point of the paper. However, we note that out of the dozen or so outflows detected, *none* come from radio continuum sources (H II regions). All outflows that have a clear origin come from millimeter-detected, centimeter-faint sources, suggesting that these sources are accreting and are not emitting ionizing radiation.

4. Discussion

4.1. The scales and types of feedback

The most prominent features of our observations are the warm, chemically enhanced regions surrounding the highest dust concentrations, and the corresponding *lack* of such features around the ionized nebulae. This difference implies that the immediate star formation process - that of gas collapse and fragmentation from a molecular cloud - is primarily affected by feedback from stars that are presently accreting and therefore emitting most of their radiation in the infrared, *not* from previous generations of now-exposed stellar photospheres.

On the scales relevant to the fragmentation process, i.e., the ~ 0.1 pc scales of prestellar cores, this decoupling can be explained simply. Stellar light is produced mostly in the UV, optical, and near-infrared. As soon as a star is exposed, either by consuming or destroying its natal core, that light is able to stream to relatively large ($\gtrsim 1$ pc) scales before being absorbed. At that point, the stellar radiation is poorly coupled to the scales of direct star formation. By contrast,

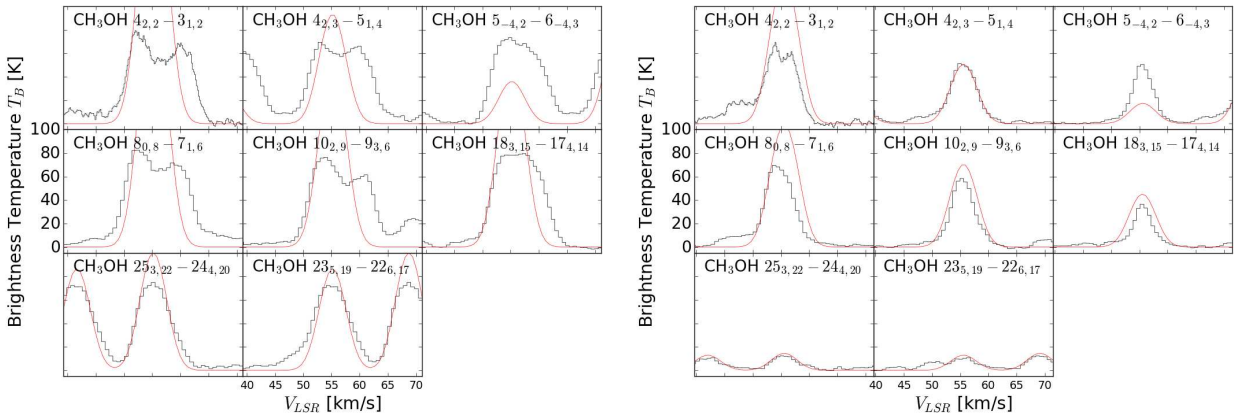

(a) (b)

Fig. 8. Spectra of the CH_3OH lines toward a pair of selected pixels just outside of the e2e core. (a) is 0.55″ and (b) is 1.33″ from e2e. The red curves show the LTE model fitted from a rotational diagram as shown in Figure 7. The model is not a fit to the data shown, but is instead a single-component LTE model fit to the integrated intensity of the lines shown. As such, the fit is not convincing, and it is evident that a single-temperature, single-velocity model does not explain the observed lines. Nonetheless, a component with the modeled temperature is likely to be present in addition to a cooler component responsible for the self-absorption in the low-J lines. (a) shows a pixel close to the center of e2e, which is probably optically thick in most of the shown transitions, while (b) shows a better case where the highest-A_{ij} lines are overpredicted but many of the others are well-fit.

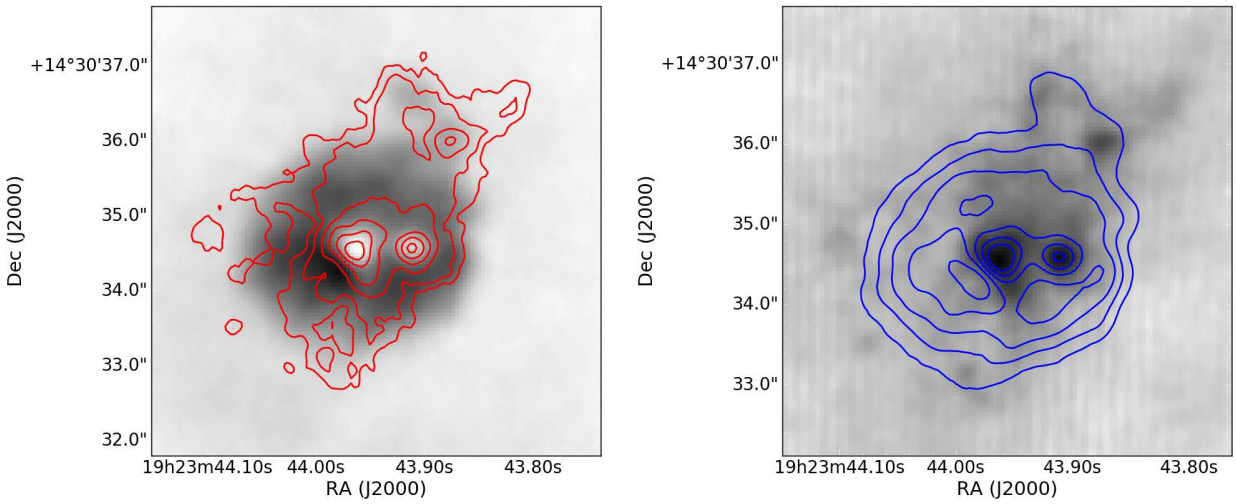

(a) (b)

Fig. 9. Images showing CH_3OH $10_{2,9} - 9_{3,6}$ and 225 GHz continuum emission, with CH_3OH in grayscale and continuum in contours (left) and continuum in grayscale, CH_3OH in contours (right). The fainter (whiter) regions in the center of the CH_3OH map correspond to the bright continuum cores and show where all lines appear to be self-absorbed.

stars embedded in their natal cores will have all of their light reprocessed from UV/optical/NIR to the far-IR within a < 0.1 pc sphere, providing a far-infrared background light capable of heating its surroundings.

The different effects of ionizing vs thermal radiation can be seen directly in the three main massive star forming regions, e2, e8, and north. Figures 14 and 15 show both the highly-excited warm molecular gas in color and the free-free emission from ionized gas in contours. As described in Section 3.6, the spatial differences indicate that the ionizing radiation sources - the exposed OB stars - have little effect on the star-forming collapsing and fragmenting gas.

The low impact of photospheric radiation on collapsing gas suggests that second-generation star formation is relatively unaffected by its surroundings. Instead, the stars of the same generation - those currently embedded and accreting - have the dominant regulating effect on the gas temperature. To the extent that gas temperature governs the IMF, then, the formation of the IMF *within clusters* is therefore predominantly self-regulated, with little external influence.

4.1.1. Hot core chemical structure

In Section 3.3, we showed regions with enhanced emission in a variety of complex chemical species over a large volume. While it is not generally correct to conclude that enhanced emission indicates enhanced abundance, the additional analysis of the CH_3OH abundance in Section 3.4

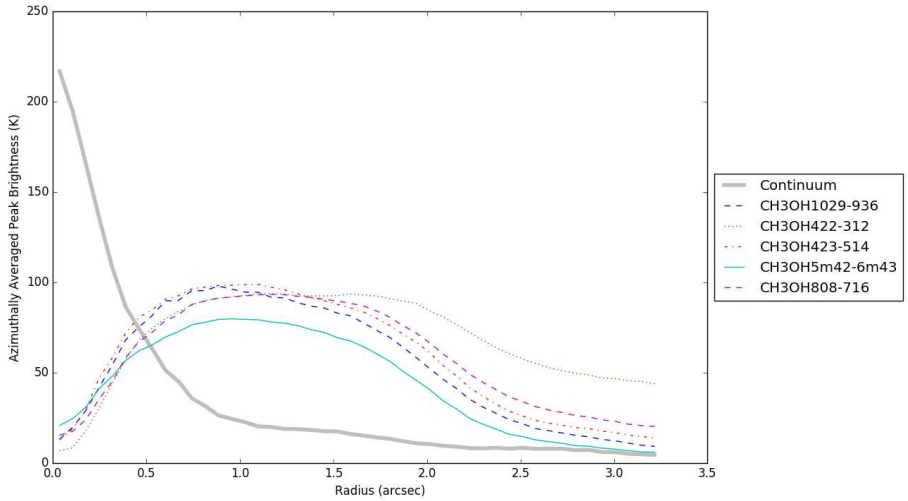

Fig. 10. Radial profiles of the peak surface brightness of five CH_3OH transitions along with the profile of the continuum brightness. The radial profiles were constructed from images with $0.2''$ resolution including only 12m data. The central dip shows where the lines go into absorption, though they are only seen in absorption at ~ 55 km s^{-1}. The CH_3OH lines are continuum-subtracted.

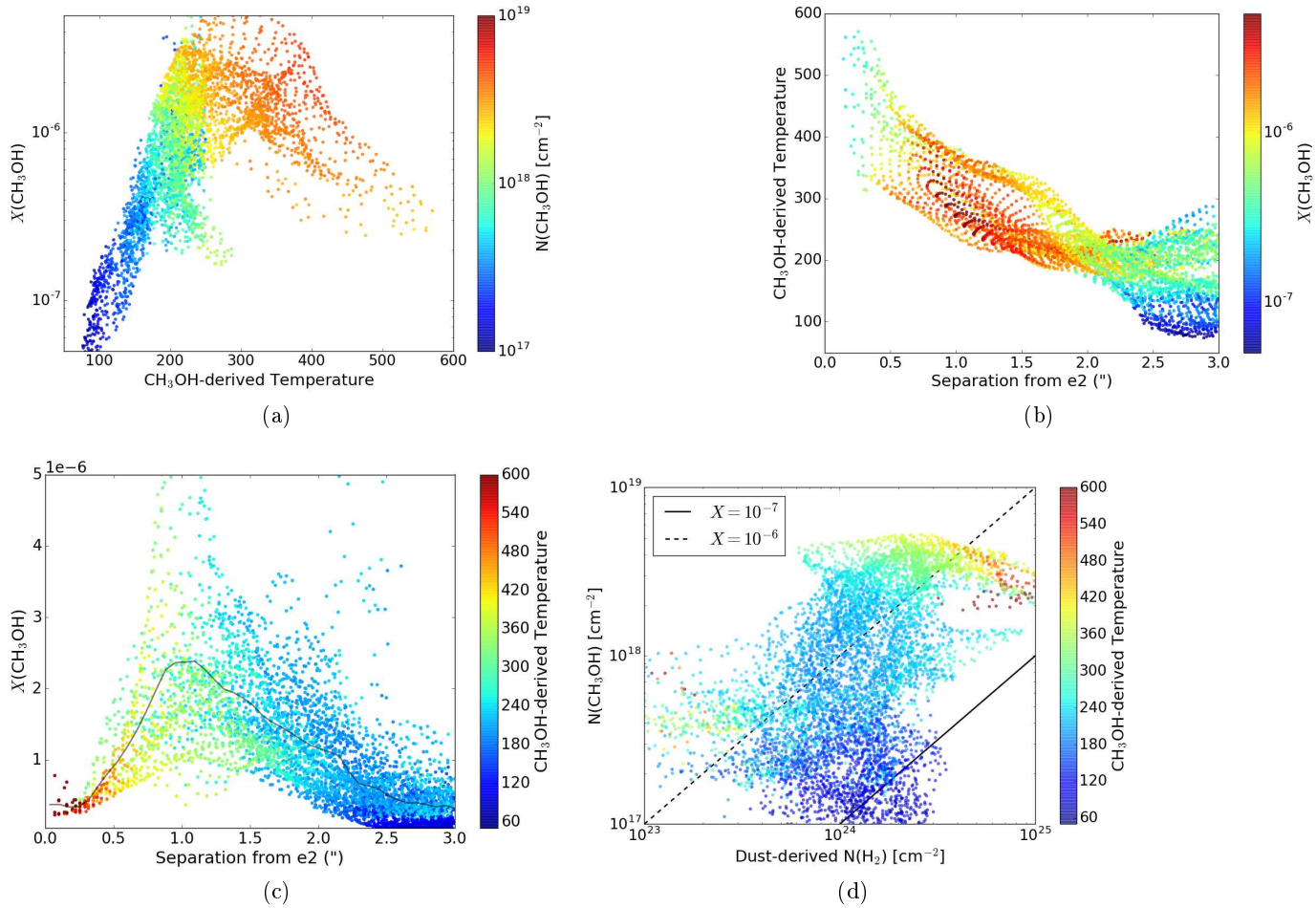

Fig. 11. Comparison of the CH_3OH temperature, column density, and abundance. (a) The relation between temperature and abundance. There is a weak correlation, but most of the high abundance regions are at high temperatures. (b) Temperature vs distance from e2e. There is a clear trend toward higher temperatures closer to the central source (c) Abundance vs distance from e2e. The apparent dip at $r < 1''$ is somewhat artificial, as it is driven by a rising dust emissivity that corresponds to an increasing optical depth in the dust. The CH_3OH column in this inner region is likely to be underestimated. (d) CH_3OH vs dust column density.

suggests that there is a genuine enhancement in complex chemical abundances toward these hot cores.

We have not performed a detailed abundance analysis of multiple species, but we nonetheless suggest that

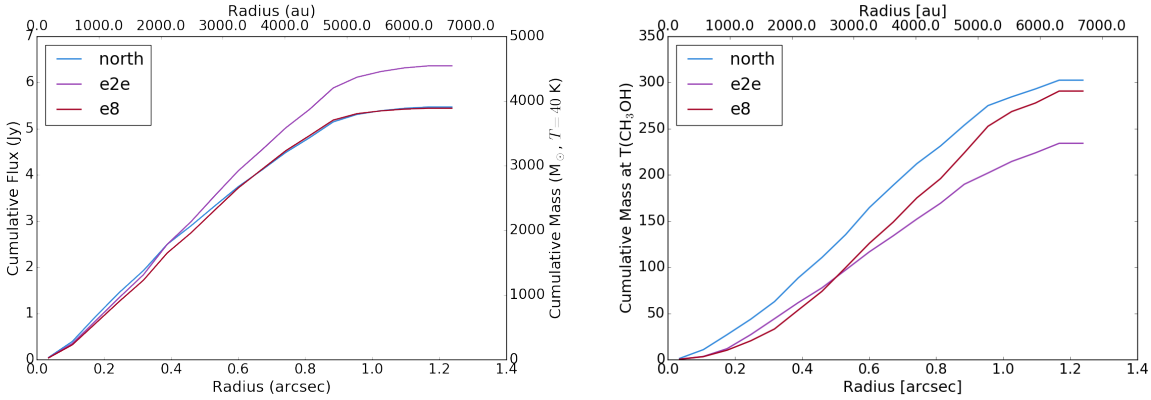

(a) (b)

Fig. 12. The cumulative (a) flux density radial profile and (b) mass radial profile centered on three massive protostellar cores. They share similar profiles and are likely dominated by hot dust in their innermost regions, but they are more likely to be dominated by cooler dust in their outer, more massive regions. The cumulative mass distribution may therefore be deceptive. In (a), we use a constant temperature to convert from flux to mass. In (b), we use the temperature map computed from CH_3OH in Section 3.4.

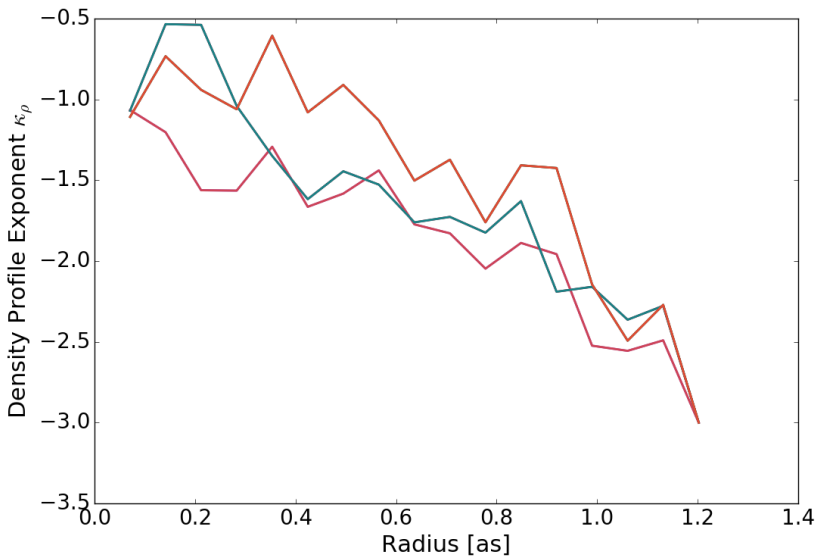

Fig. 13. The radial mass profile exponent κ_ρ as a function of radius. The 'fiducial value' used in the McKee & Tan (2003) model is $\kappa_\rho = 1.5$, but importantly it is *constant* at $t = 0$. A non-constant κ_ρ indicates that collapse is not self-similar, and the flattening toward smaller radii suggests that it is slower than freefall collapse.

these sharp-edged bubbles around the hot cores represent sublimation zones in which substantial quantities of grain-processed materials are released into the gas phase. The relatively sharp edges likely reflect the particular point where the temperature exceeds the sublimation temperature for each species (Garrod et al. 2006), though some species may appear at temperatures above or below their sublimation temperature if they are mixed into ices that have a different sublimation temperature.

Most of the lines identified in the hot cores e2e, e8, and north are also present in ALMAmm14. However, their extent is greater toward the more luminous sources. An examination of the relationship between the luminosity of the protostars and the extent of their chemically enhanced zones will be useful for identifying further very massive protostars.

4.1.2. Outflows

While the outflows described in Section B are impressive and plentiful, they are obviously not the dominant form of feedback, as their area filling factor is small compared to that of the various forms of radiative feedback. A low area filling factor implies a substantially smaller volume filling factor and therefore a lower overall effect on the cloud. However, these outflows likely do punch holes through protostellar envelopes and the surrounding cloud material, allowing radiation to escape.

The detection of widespread high-J CH_3OH emission around the highest-mass protostars suggests that the use of CH_3OH as a bulk outflow tracer as suggested by Kristensen & Bergin (2015) is not viable in regions with forming high-mass stars. While mid-J CH_3OH emission is detected associated with the outflow (e.g., the J=10-9 transition), it

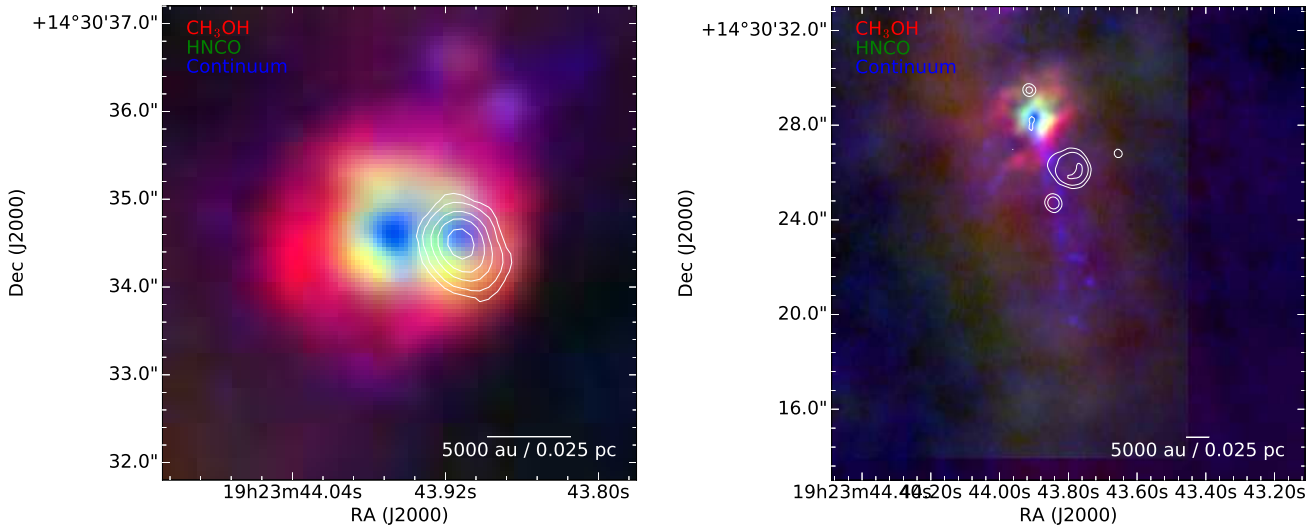

(a) (b)

Fig. 14. Image of CH_3OH $8_{0,8} - 7_{1,6}$ (red), HCNO $10_{0,10} - 9_{0,9}$ (green), and 225 GHz continuum (blue) toward (a) W51e2 (b) W51e8. The contours show Ku-band radio continuum emission tracing the H II regions (a) W51 e2w and (b) W51e1, e3, e4, e9, and e10. The CH_3OH emission is relatively symmetric around the high-mass protostar W51 e2e and the weak radio source W51 e8, suggesting that these forming stars are responsible for heating their surroundings. By contrast, the H II regions do not exhibit any local molecular brightness enhancements (except e8), indicating that the H II regions are not heating their local dense molecular gas.

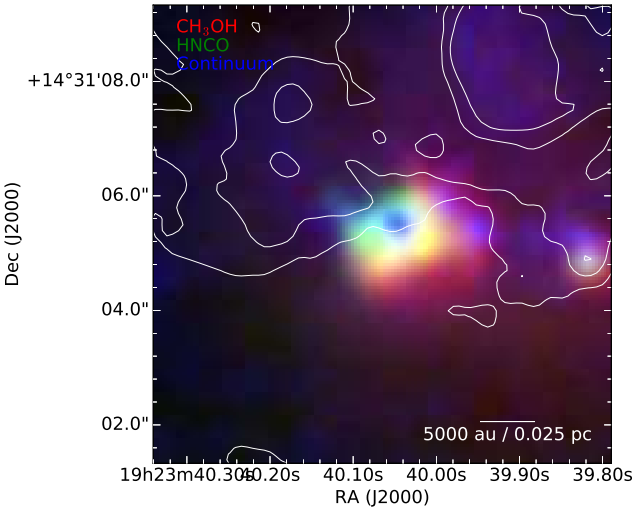

Fig. 15. Image of CH_3OH $8_{0,8} - 7_{1,6}$ (red), HCNO $10_{0,10} - 9_{0,9}$ (green), and 225 GHz continuum (blue) toward north, as in Figure 14. The contours show Ku-band radio continuum emission tracing the diffuse IRS 2 H II region.

is completely dominated by the general 'extended hot core' emission described in Section 3.3.

None of the outflows initiate in UCH II or HCH II regions. While a clear origin cannot be determined for all of the outflows, it is clear that no cm continuum sources lay at the base of any. The lack of molecular outflows toward these sources implies that they are accreting at most weakly or are accreting (and ejecting) only atomic or ionized material.

4.2. The accreting phase of high-mass star formation

The strong outflows observed around the highest-mass forming stars, e2e, e8, and north are clear indications of ongoing accretion onto these sources. However, the bright H II regions, including e2w, e1, and d2, all lack any sign of an outflow or a surrounding rotating molecular structure. Most of these sources lack any surrounding molecular material at all.

Some models of high-mass star formation suggest that accretion continues through the ionized (H II region) phase (e.g. Keto 2007). The lack of molecular material around the majority of the compact H II regions in W51 suggests instead that most of the accretion is done by the time an H II region ignites.

There is one counterexample in our sample. The source d2 is a bright, compact H II region, but it is also surrounded by a molecular enhancement. However, it does not appear to drive an outflow, so there is again no direct evidence of ongoing accretion.

The correlation of the extended hot cores with outflow-driving source suggests that the heating of these hot cores is either from accretion luminosity, or that the high accretion rate indicated by the presence of outflows is necessary to reprocess stellar photospheric light into the infrared.

4.3. The accreting stars

In Sections ?? and 3.1.2, we noted that the *lower limit* luminosities for the three most massive cores correspond to early B-type photospheres. Such stars should emit enough radiation to ignite luminous compact H II regions.The upper limits on the presence of such an H II region are constraining, with $R < 100AU$, which is consistent with the presence of these stars, but inconsistent with any hotter or more luminous (spectral type <B0.5V). If the stellar luminosities are an order of magnitude or more higher, which is possible given the low-resolution constraints on the bolometric luminosity (Ginsburg et al. 2016b; Sievers et al. 1991) and likely if a large fraction of the stellar radiation is escaping along outflow cavities (Kuiper & Yorke 2012; Zhang et al. 2013), the luminosity would be too large and the UV radiation too small to be consistent with a main-sequence OB star.

Since we can provide only upper limits on the UV radiation, it is possible that there is none at all. The very large mass reservoir suggests that high accretion rates are possible, and the bright molecular outflows show that accretion is proceeding vigorously (though we have not quantified the rate). Rapid accretion, and in particular rapid and *variable* accretion, can change the properties of the underlying star, bloating the star and reducing its effective photospheric temperature (Hosokawa & Omukai 2009; Smith et al. 2012; Hosokawa et al. 2016). Such stars can achieve radii $R \gtrsim 200R_\odot \sim 1$ AU while retaining photospheric temperatures $T \lesssim 5000$ K. We hope to explore this possibility further in a subsequent paper.

4.4. Fragmentation: Jeans analysis

Fragmentation is one of the critical problems in high-mass star formation. Assuming typical initial conditions for molecular clouds, with temperatures of order 10 K, gas is expected to fragment into sub-solar mass cores, preventing material from accreting onto single high-mass stars (Krumholz et al. 2015). Even after high-mass stars successfully form, further fragmentation could halt the growth of these stars and limit their final mass (Peters et al. 2010b).

Thermal Jeans fragmentation can be limited or suppressed entirely if the gas is warm enough. The high observed gas temperatures, $T \sim 100 - 600$ K over $\sim 10^4$ AU, around the high mass protostars indicate that their radiative feedback in the infrared has a dramatic effect on the gas. The heated region qualitatively matches that of Krumholz (2006), who described a core heated only by accretion luminosity down to $R = 10$ AU and therefore gave a lower limit on the total heating.

We examined the temperature structure around the highest-mass cores in Section C.3 and the mass structure in Section 3.5. We put these together to measure the Jeans mass, $M_J = (\pi/6)c_s^3 G^{-3/2}\rho^{-1/2}$, and length, $\lambda_J = c_s G^{-1/2}\rho^{-1/2}$, in Figure 16. These plots show the *radially averaged* M_J and $R_J = \lambda_J/2$, i.e., they show the Jeans mass and length if the medium were of uniform density and temperature at the spherical-shell-average density and azimuthal average temperature at each plotted radius. Interpretation of these plots is not straightforward, though: if we assume the 'core' is spherically symmetric, the intersection of our telescope beam (which is approximately cylindrical) with the core is highly nontrivial: if the core has a profile $\kappa_\rho < 2$, the observed mass will greatly exceed the spherical shell mass at large radii, while if $\kappa_\rho > 2$, it will be an underestimate at some radii.

The high gas temperature therefore provides a mechanism for MYSOs to avoid the "fragmentation-induced starvation" problem discussed by Peters et al. (2010b,a); Girichidis et al. (2012). Apparently, stars above some mass are able to heat hundreds of $M_\odot$ of material surrounding them to such a degree that it cannot fragment further, providing an enormous reservoir to feed from.

Within this large reservoir, there are few currently-detected fragments. In our data, within 6500 AU of W51 north, there is only 1 (ALMAmm35), around e2e there is the HII region e2w and possibly 2-3 others between 5000 and 6500 AU, and around e8 there are none. Admittedly, our data are not very sensitive in the areas immediately surrounding these cores because of dynamic range limitations, but the higher Jeans mass noted above suggests that any fragments that do exist should be more massive and therefore more detectable.

Further fragmentation below 1000 AU is possible, e.g., as seen in NGC 6334Imm1 (Brogan et al. 2016). However, in the long baseline data to be presented in a future work (Goddi et al, in prep), very little additional fragmentation is observed. A few more sources are detected toward e2e and north and many toward e8, but the nature of those more compact (< 200 AU) sources suggests they are protostellar or stellar. Additionally, unlike the centrally-clustered fragmentation seen in NGC 6334Imm1, the fragments that are detected appear spread out in W51.

By suppressing fragmentation in their surroundings, accreting massive stars are able to sustain their mass reservoir. They effectively create their own cores. Given the current structure of the observed cores and their marginal stability against fragmentation, it is unlikely that these cores could have existed at all without the presence of a central heating source. Should these > 200 $M_\odot$ cores have been present before high-mass star formation initiated, resting at $T \sim 20$ K as in a typical molecular cloud, they would have been subject to Jeans fragmentation on a much smaller scale and would have formed a cluster of smaller stars. This implies that the mass currently in the core had to be assembled from larger scales while suppressing or slowing collapse on smaller scales, which is essentially the opposite of inside-out collapse.

4.5. High-mass star formation within dense protoclusters

Since massive ($M \gtrsim 250$ $M_\odot$) hot cores presently exist, and they appear to be the precursors to a next generation of high mass stars, there is a clear route to high-mass star formation given the presence of strong feedback sources. However, this raises the question of what the initial conditions were. Did the current generation of forming massive stars start life the same way as previous generations?

One possibility hinted at by the density of hyper- and ultra-compact H II regions around each of the massive cores

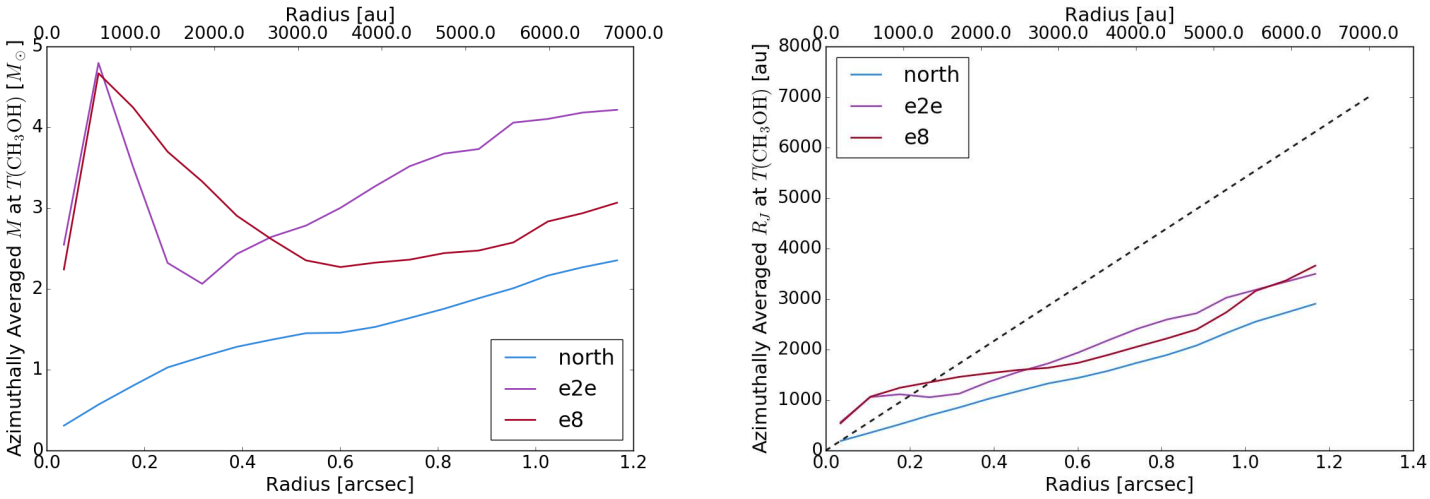

Fig. 16. The azimuthally averaged (a) Jeans mass and (b) Jeans length surrounding the three most massive cores. We used the CH_3OH temperature from 3.4, Figure 12b in both the Jeans mass calculation and the dust-based mass determination. The density used for the mass calculation is assumed to be distributed over spherical shells. In (b), the dashed black line shows the $R_J = R$ line. When $R_J > R$, the gas is on average stable against fragmentation on the measured length scale. Since the medium is clearly *not* isothermal or uniform density, though, this only shows a rough approximation of the stability.

is that they did not. Heating from previous generations of moderate mass stars could have warmed the gas, suppressing fragmentation into the sub-solar mass objects typical in local clouds until enough gas was present to collapse into a substantially larger object. This toy model is analagous to the 'cooperative accretion' mode suggested by Zinnecker & Yorke (2007), but at a much earlier stage in the cluster development when the gas is still molecular and dusty and therefore capable of efficient cooling. It is also similar to the results of Krumholz et al. (2011), in which radiative heating drove up the peak of the IMF; in this case, though, we suggest that the affected region is smaller (not the whole cloud) and that the "top-heavy IMF" is a solution, not a problem.

In this scenario, the highest mass stars (probably "very massive stars", $M \gtrsim 50\ M_\odot$) would only be capable of forming within dense, clustered environments, since larger stars would be prevented from forming by earlier fragmentation elsewhere. The IMF would then be built up by an inverse hierarchy, with progressively larger stars capable of forming over time until the gas is either exhausted (Ginsburg et al. 2016a) or expelled.

However, some of the assumptions in this scenario contradict our observations. If the previous generation were responsible for substantial gas heating, we might expect to see warm gas surrounding the HCH II regions. Instead, we see these stars barely interacting with the dense gas. However, it is possible that these stars are only effective at dense gas heating *before* they ignite Lyman continuum emission and blow out cavities, and afterward they are merely uninteractive witnesses to continued collapse.

The alternatives to this hypothesis are that the initial conditions were entirely set within the gas on these current scales, which seems implausible, or that the current high density of main-sequence stars (i.e., the observed HCH II regions) originated from a broader, lower-density distribution and dynamically collapsed into their current clustered state. If the stars illuminating HCH II regions formed somewhat earlier in a more distributed manner and fell into a common central potential, they would have had little effect on the dense gas temperature.

4.6. Comparison to high-mass star formation theories

Two general classes of star formation theory, "competitive accretion" and "turbulent core accretion" have dominated the discussion of high-mass star formation, though they are not fully complementary theories (Schilke 2016). In their extreme forms, they can be simplified to uniform seeds accreting different amounts of material over their lifetime in the case of competitive accretion and a single, initial, quasistatic high-mass gas core collapsing into a star in the case of turbulent core accretion.

Our observations of high-mass hot cores extending to radii ~ 5000 AU do not directly contradict either of these extremes, but instead suggests that the accretion models used within these theories must be modified.

If there are many simultaneously formed low-mass fragments competing for material, as in competitive accretion, it appears that the formation of a dominant most massive star dramatically changes the conditions for accretion. This single central source heats material enough to reduce the efficiency of Bondi-Hoyle accretion by a factor of 10 for a stationary object, though the reduction is negligible for an object moving near the Virial velocity ($v_{vir} \gtrsim 5$km s^{-1} within the hot cores). However, this extended warm region suppresses the formation of new small fragments, as has been observed in simulations with much weaker feedback (e.g. Bate 2009). It is not clear whether the mass accumulated around the most massive protostars at present came from large radii, as in Smith et al. (2009), but it is certainly possible.

If the turbulent core model is used to describe these sources, a few obvious issues arise. First, the core structure is not a simple power-law with $\kappa_\rho = 1.5$, as usually assumed (McKee & Tan 2003; Zhang & Tan 2011). Fig-

ure 13 shows instead that the core is internally flatter and externally steeper than this assumption. Of course, the observations do not correspond to the initial conditions, so this comparison could more fairly be made with a later 'snapshot' from those models. Second, the more sophisticated models of evolution from an initial turbulent core suggest that most of the stellar (and accretion) radiation should escape via growing outflow cavities (Zhang & Tan 2011; Zhang et al. 2013, 2014). The circular symmetry seen in the hot core around e2e and its lack of correspondence with the outflowing material (Figure 17) indicates that a large fraction of the stellar or accretion radiation is going directly into the core and not escaping along the poles.

The presence of these large-scale, massive, hot cores raises a few questions that are not presently well-addressed by any class of theories. If the hot cores successfully suppress further fragmentation in their envelopes, does that imply that these cores will collapse into single stars? If so, do the cores in any way correspond to 'initial conditions', or are the cores created by the stars that form within them? This is more than merely a semantical question, as the evolutionary progress within the 'turbulent core' model depends on the initial core structure, and the presence of nearby fragments governs whether 'competitive accretion' can occur at all.

this is mostly just spitballing; it probably ought to be removed: There are also some curious implications for 'isolated' massive star formation. The stars we see forming are clearly not isolated - they are embedded within fairly rich clusters of massive stars we can see already, and they are very likely to be surrounded by substantial clusters of lower-mass stars. However, *during their formation process*, they may be the only accreting stars around - their thermal feedback may prevent any neighbors from forming simultaneously. This 'enforced isolation' might be a way for massive star formation to proceed similarly independent of the size of their parent cloud, assuming they can be formed at all.

4.7. Low-mass star formation in and around the MYSOs

? observed a region in which high-mass and low-mass star formation is occurring concurrently. The same is almost certainly occurring in W51. Is there more to say here?

5. Conclusions

We have presented ALMA observations of the high-mass protocluster W51. We examined the three most massive forming stars and the surrounding population of forming stars.

The key observational results include:

- We demonstrated three techniques for estimating the temperature of dust continuum sources with ALMA: limits from dust brightness temperature, limits from line brightness temperature, and LTE modeling of CH_3OH lines. While these methods do not necessarily agree or provide direct and accurate measurements of the temperature, they provide strong enough constraints to draw substantial physical conclusions.
- We cataloged and classified 75 continuum sources on the basis of their dust emission, line emission, and morphology.
- We identified chemically enhanced regions around high-mass protostars and suggest they are desorption zones

From these observations, we have inferred the following:

- During the earliest stages of their formation, before they have ignited H II regions, high-mass protostars heat a large volume, and correspondingly large mass, of gas around them.
- Older massive stars, those with surrounding H II regions, appear to have little effect on the temperature of dense gas around them. While some are embedded within larger hot cores, they do not appear to be the main heating sources. Their luminosity must therefore escape without being fully reprocessed into infrared radiation.
- Heated massive cores surrounding the highest-mass protostars in W51 show no evidence of ongoing fragmentation and are warm enough to suppress Jeans fragmentation. Hot massive cores therefore serve as a mass reservoir for accretion onto possibly single massive stars.

Acknowledgments The National Radio Astronomy Observatory is a facility of the National Science Foundation operated under cooperative agreement by Associated Universities, Inc. This paper makes use of the following ALMA data: 2013.1.00308.S and 2015.1.01596.S. ALMA is a partnership of ESO (representing its member states), NSF (USA) and NINS (Japan), together with NRC (Canada), NSC and ASIAA (Taiwan), and KASI (Republic of Korea), in cooperation with the Republic of Chile. The Joint ALMA Observatory is operated by ESO, AUI/NRAO and NAOJ. JMDK gratefully acknowledges funding in the form of an Emmy Noether Research Group from the Deutsche Forschungsgemeinschaft (DFG), grant number KR4801/1-1.

Code Packages Used:

- CASA https://casa.nrao.edu/
- pyspeckit http://pyspeckit.bitbucket.org Ginsburg & Mirocha (2011)
- aplpy https://aplpy.github.io/
- wcsaxes http://wcsaxes.readthedocs.org
- spectral cube http://spectral-cube.readthedocs.org
- ds9 http://ds9.si.edu
- dust_emissivity dust_emissivity.readthedocs.org

References

Aguirre, J. E. et al. 2011, ApJS, 192, 4
Barbosa, C. L., Blum, R. D., Conti, P. S., Damineli, A., & Figuerêdo, E. 2008, ApJ, 678, L55
Bastian, N., Covey, K. R., & Meyer, M. R. 2010, ARA&A, 48, 339
Bate, M. R. 2009, MNRAS, 397, 232
—. 2012, MNRAS, 419, 3115
Bate, M. R., Tricco, T. S., & Price, D. J. 2014, MNRAS, 437, 77
Beltrán, M. T. & de Wit, W. J. 2016, A&A Rev., 24, 6
Brogan, C. L., Hunter, T. R., Cyganowski, C. J., Chandler, C. J., Friesen, R., & Indebetouw, R. 2016, ArXiv e-prints
Crowther, P. A. et al. 2016
De Pree, C. G. et al. 2014, ApJ, 781, L36
Eisner, J. A., Greenhill, L. J., Herrnstein, J. R., Moran, J. M., & Menten, K. M. 2002, ApJ, 569, 334
Forgan, D. H., Ilee, J. D., Cyganowski, C. J., Brogan, C. L., & Hunter, T. R. 2016, ArXiv e-prints
Garrod, R. T., Williams, D. A., & Rawlings, J. M. C. 2006, MNRAS, 373, 577

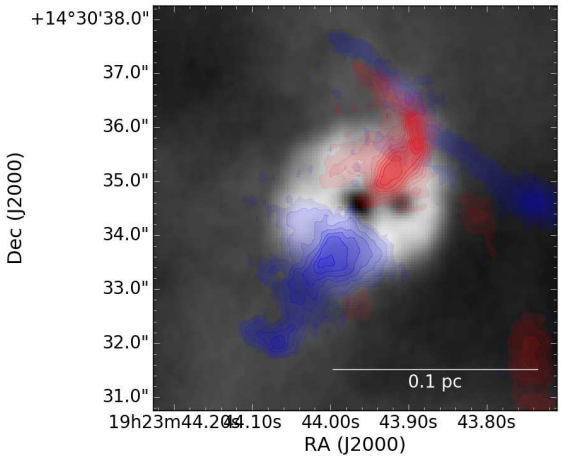

Fig. 17. The e2e core as seen in the CH_3OH $8_{0,8} - 7_{1,6}$ line with the integrated ^{12}CO outflow overlaid in red and blue. The 'core' is circularly symmetric, while the outflow is clearly bipolar.

Ginsburg, A., Bally, J., Battersby, C., Youngblood, A., Darling, J., Rosolowsky, E., Arce, H., & Lebrón Santos, M. E. 2015, A&A, 573, A106
Ginsburg, A., Bressert, E., Bally, J., & Battersby, C. 2012, ApJ, 758, L29
Ginsburg, A. et al. 2013, ApJS, 208, 14
—. 2016a, A&A, 595, A27
—. 2016b, A&A, 586, A50
Ginsburg, A. & Mirocha, J. 2011, PySpecKit: Python Spectroscopic Toolkit, Astrophysics Source Code Library
Girichidis, P., Federrath, C., Banerjee, R., & Klessen, R. S. 2012, MNRAS, 420, 613
Goddi, C., Ginsburg, A., & Zhang, Q. 2016
Harvey, P. M., Joy, M., Lester, D. F., & Wilking, B. A. 1986, ApJ, 300, 737
Hodapp, K. W. & Davis, C. J. 2002, ApJ, 575, 291
Hosokawa, T., Hirano, S., Kuiper, R., Yorke, H. W., Omukai, K., & Yoshida, N. 2016, ApJ, 824, 119
Hosokawa, T. & Omukai, K. 2009, ApJ, 691, 823
Keto, E. 2007, ApJ, 666, 976
Klassen, M., Pudritz, R. E., Kuiper, R., Peters, T., & Banerjee, R. 2016, ApJ, 823, 28
Koch, P. M., Tang, Y.-W., & Ho, P. T. P. 2010, ApJ, 721, 815
—. 2012a, ApJ, 747, 79
—. 2012b, ApJ, 747, 80
Kristensen, L. E. & Bergin, E. A. 2015
Kroupa, P. 2001, MNRAS, 322, 231
Krumholz, M. R. 2006, ApJ, 641, L45
Krumholz, M. R., Fumagalli, M., Silva, R. L. d., Rendahl, T., & Parra, J. 2015
Krumholz, M. R., Klein, R. I., & McKee, C. F. 2007, ApJ, 656, 959
—. 2011, ApJ, 740, 74
Krumholz, M. R., Klein, R. I., McKee, C. F., Offner, S. S. R., & Cunningham, A. J. 2009, Science, 323, 754
Krumholz, M. R. & Matzner, C. D. 2009, ApJ, 703, 1352
Krumholz, M. R., McKee, C. F., & Klein, R. I. 2005, ApJ, 618, L33
Kuiper, R., Turner, N. J., & Yorke, H. W. 2016
Kuiper, R. & Yorke, H. W. 2012, ArXiv e-prints
—. 2013, ApJ, 763, 104
Kuiper, R., Yorke, H. W., & Turner, N. J. 2015, ApJ, 800, 86
Lacy, J. H. et al. 2007, ApJ, 658, L45
McKee, C. F. & Tan, J. C. 2003, ApJ, 585, 850
Molinari, S. et al. 2016, ArXiv e-prints
Offner, S. S. R., Lee, E. J., Goodman, A. A., & Arce, H. 2011, ApJ, 743, 91
Ossenkopf, V. & Henning, T. 1994, A&A, 291, 943
Parker, R. J. & Goodwin, S. P. 2007, MNRAS, 380, 1271
Pecaut, M. J. & Mamajek, E. E. 2013, ApJS, 208, 9
Peters, T., Banerjee, R., Klessen, R. S., Mac Low, M.-M., Galván-Madrid, R., & Keto, E. R. 2010a, ApJ, 711, 1017
Peters, T., Klessen, R. S., Mac Low, M.-M., & Banerjee, R. 2010b, ApJ, 725, 134
Rosen, A. L., Krumholz, M. R., McKee, C. F., & Klein, R. I. 2016
Rosolowsky, E. W., Pineda, J. E., Kauffmann, J., & Goodman, A. A. 2008, ApJ, 679, 1338
Sato, M., Reid, M. J., Brunthaler, A., & Menten, K. M. 2010, ApJ, 720, 1055
Schilke, P. 2016
Shi, H., Zhao, J.-H., & Han, J. L. 2010a, ApJ, 718, L181
—. 2010b, ApJ, 710, 843
Sievers, A. W., Mezger, P. G., Bordeon, M. A., Kreysa, E., Haslam, C. G. T., & Lemke, R. 1991, A&A, 251, 231
Smith, R. J., Hosokawa, T., Omukai, K., Glover, S. C. O., & Klessen, R. S. 2012, MNRAS, 424, 457
Smith, R. J., Longmore, S., & Bonnell, I. 2009, MNRAS, 400, 1775
Tang, Y.-W., Ho, P. T. P., Koch, P. M., Girart, J. M., Lai, S.-P., & Rao, R. 2009, ApJ, 700, 251
Tang, Y.-W., Ho, P. T. P., Koch, P. M., Guilloteau, S., & Dutrey, A. 2012, ArXiv e-prints
Wang, K., Testi, L., Ginsburg, A., Walmsley, C. M., Molinari, S., & Schisano, E. 2015, MNRAS, 450, 4043
Yorke, H. W. & Sonnhalter, C. 2002, ApJ, 569, 846
Zapata, L. A., Ho, P. T. P., Schilke, P., Rodríguez, L. F., Menten, K., Palau, A., & Garrod, R. T. 2009, ApJ, 698, 1422
Zapata, L. A., Tang, Y.-W., & Leurini, S. 2010, ApJ, 725, 1091
Zhang, Q. & Ho, P. T. P. 1997, ApJ, 488, 241
Zhang, Y. & Tan, J. C. 2011, ApJ, 733, 55
Zhang, Y., Tan, J. C., & Hosokawa, T. 2014, ApJ, 788, 166
Zhang, Y., Tan, J. C., & McKee, C. F. 2013, ApJ, 766, 86
Zinnecker, H. & Yorke, H. W. 2007, ARA&A, 45, 481

Appendix A: A bubble around e5

There is evidence of a bubble in the continuum around e5 with a radius of 6.2″ (0.16 pc; Figure A.1). The bubble is completely absent in the centimeter continuum, so the observed emission is from dust. The bubble edge can be seen from 58 km s^{-1} to 63 km s^{-1} in $C^{18}O$ and H_2CO, though it is not continuous in any single velocity channel. There is a collection of compact sources (protostars or cores) along the southeast edge of the bubble.

The presence of such a bubble in dense gas, but its absence in ionizing gas, is surprising. The most likely mechanism for blowing such a bubble is ionizing radiative feedback, especially around a source that is currently a hypercompact HII region, but since no free-free emission is evident within or on the edge of the bubble, it is at least not presently driving the bubble. A plausible explanation for this discrepancy is that e5 was an exposed O-star within the past Myr, but has since begun accreting heavily and therefore had its HII region shrunk. This model is marginally

supported by the presence of a 'pillar' of dense material pointing from e5 toward the south.

The total flux in the north half of the 'bubble', which shows no signs of free-free contamination, is about 1.5 Jy. The implied mass in just this fragment of the bubble is about $M \sim 350\ M_\odot$ for a relatively high assumed temperature $T = 50$ K. The total mass of the bubble is closer to $M \sim 1000\ M_\odot$, though it may be lower ($\sim 500\ M_\odot$) if the southern half is dominated by free-free emission.

With such a large mass, the implied density of the original cloud, assuming it was uniformly distributed over a 0.2 pc sphere, is $n(\mathrm{H_2}) \approx 2 - 5 \times 10^5\ \mathrm{cm^{-3}}$.

To evaluate the plausibility of the H II-region origin of the bubble, we compare to classical equations for H II regions. The Strömgren radius is

$$R_\mathrm{s} = \left(\frac{3Q_\mathrm{H}}{4\pi\alpha_\mathrm{B}n^2}\right)^{\frac{1}{3}}. \tag{A.1}$$

For $Q_\mathrm{H} \sim 10^{49}\ \mathrm{s^{-1}}$, $\alpha_\mathrm{B} = 3 \times 10^{-13}\,\mathrm{cm^3\,s^{-1}}$, $R_\mathrm{s} \approx 0.01\,\mathrm{pc}$.

The Spitzer solution for HII region expansion gives

$$R_\mathrm{HII}(t) = R_\mathrm{s}\left(1 + \frac{7}{4}\frac{c_\mathrm{II}t}{R_\mathrm{s}}\right)^{\frac{4}{7}}. \tag{A.2}$$

With $c_\mathrm{II} = 7.5\,\mathrm{km\,s^{-1}}$ and $t = 10^4\,\mathrm{yr}$, $R_\mathrm{HII}(t) \approx 0.04\,\mathrm{pc}$, while at $t = 10^5\,\mathrm{yr}$, it is $R_\mathrm{HII} \approx 0.16\,\mathrm{pc}$, which is comparable to the observed radius ($r_{obs} \sim 0.13 - 0.19$ pc)

Whitworth et al. 1994 give the fragmentation timescale as

$$t_\mathrm{frag} \sim 1.56\left(\frac{c_\mathrm{s}}{0.2\mathrm{km\,s^{-1}}}\right)^{\frac{7}{11}}\left(\frac{Q_\mathrm{H}}{10^{49}\mathrm{s^{-1}}}\right)^{-\frac{1}{11}}\left(\frac{n}{10^3\mathrm{cm^{-3}}}\right)^{-\frac{5}{11}} \tag{A.3}$$

Plugging in our numbers gives $t_\mathrm{frag} \approx 1.0 \times 10^5\,\mathrm{yr}$, or 10× longer than the expansion time.

These values are consistent with a late O-type star having been exposed, driving an H II region, for $\sim 10^4 - 10^5$ year, after which a substantial increase in the accretion rate quenched the ionizing radiation from the star, trapping it into a hypercompact ($r < 0.005$ pc) configuration. The recombination timescale is short enough that the ionized gas would disappear almost immediately after the continuous ionizing radiation source was hidden. This is essentially the scenario laid out in De Pree et al. (2014) as an explanation for the compact H II region lifetime problem. In this case, however, it also seems that the H II region has effectively driven the "collect" phase of what will presumably end in a collect-and-collapse style triggering event.

Technically, it is possible that e5 actually represents an optically thick high-mass-loss-rate wind rather than an ultracompact HII region. For example, η Car would have a flux of ~ 0.5 Jy at 2 cm and ~ 5 Jy at 1 mm at the distance of W51. While we cannot rule out this possibility, it would render the association of e5 with the 'bubble' purely coincidental.

Appendix B: Outflows

We detected many outflows, primarily in CO 2-1 and SO $6_5 - 5_4$. The flows are weakly detected in some other lines, e.g. $\mathrm{H_2CO}$, but we defer discussion of outflow chemistry to a future work.

In this section, we discuss some of the unique outflows and unique features of outflows in the W51 region. We show the most readily identified outflows in Figures B.3, B.2, B.4, and B.5.

Appendix B.0.1: The Lacy jet

A high-velocity outflow was discovered within the W51 IRS2 region by Lacy et al. (2007), and subsequently detected in H77α by Ginsburg et al. (2016a). We have discovered the CO counterpart to this outflow, which comes from near the continuum source ALMAmm31 (Figure B.1). Strangely, though, the outflow is not directly centered on the millimeter continuum source, but is slightly offset. The outflow shows red- and blue-shifted lobes that form the base of the ionized outflow reported by Lacy et al. (2007, Figure B.2).

The presence of the Lacy jet is important for ruling out outflows from H II regions. It provides clear evidence that a molecular outflow that is subsequently ionized can be easily detected in existing radio recombination line data. If outflows of comparable mass were being launched from the stars at the centers of HCH II regions (e.g., e2w), we would detect these flows. Their absence provides an upper limit on the outflow rate - and presumably the accretion rate - onto these sources. While we cannot yet make that limit quantitative, it is clear that the HCH II region sources are accreting substantially less than the dust continuum sources.

Appendix B.0.2: north

The outflow from W51 north is extended and complex. A jet-like high-velocity feature appears directly to the north of W51 north in both CO and SO (Figure B.2). However, in SO, this feature begins to emit at ~ 47 km s^{-1} and continues to ~ 100 km s^{-1}. The CO emission below < 70 km s^{-1} is completely absent, presumably obscured by foreground material. The blueshifted component, by contrast with the red, points to the southeast and is barely detected in CO, but again cleanly in SO. It is sharply truncated, extending only $\sim 1''$ (~ 5000 AU). Unlike the Lacy jet, there is no evidence that this outflow transitions into an externally ionized state.

The northernmost point of the W51 North outflow may coincide with the Hodapp & Davis (2002) $\mathrm{H_2}$ and [Fe II] outflow. There is some CO 2-1 emission coincident with the southernmost point of the $\mathrm{H_2}$ features, and these all lay approximately along the W51 North outflow vector. However, the association is only circumstantial.

Appendix B.0.3: The e2e outflow

The dominant outflow in W51, which was previously detected by the SMA (Shi et al. 2010b,a), comes from the source e2e. This outflow is remarkable for its high velocity, extending nearly to the limit of our spectral coverage in ^{12}CO. The ends of the flow cover at least $-50 < v_{lsr} < 160$ km s^{-1}, or a velocity $v \pm 100$ km s^{-1}.

The morphology is also notable. Both ends of the outflow are sharply truncated at $\sim 2.5''$ (0.07 pc) from e2e

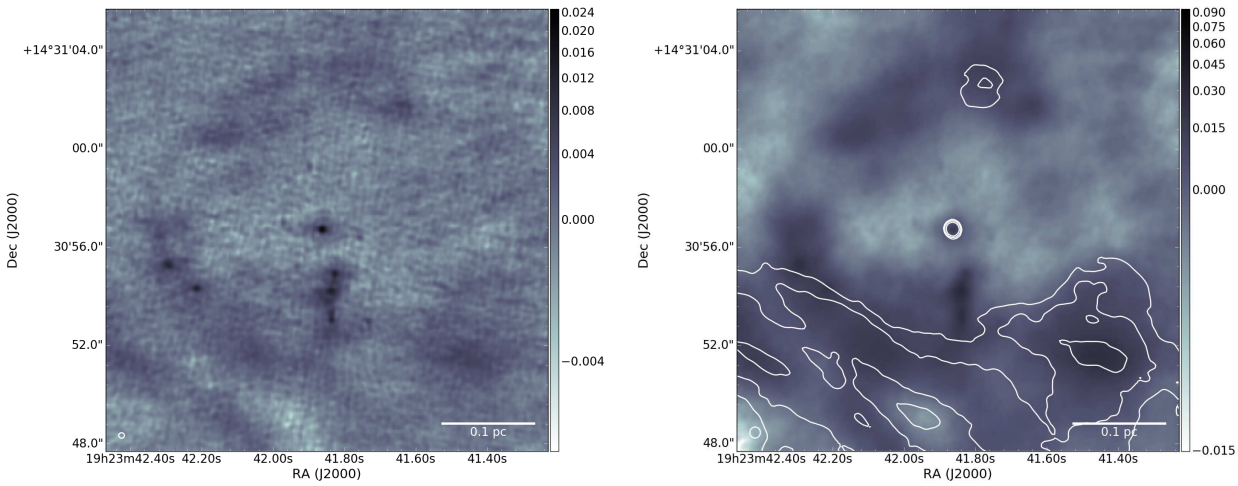

(a) (b)

Fig. A.1. The bubble around source e5. The bubble interior shows no sign of centimeter emission, though the lower-left region of the shell - just south of the "cores" - coincides with part of the W51 Main ionized shell. The source of the ionization is not obvious. (*Left*): A robust -2.0 image with a small (0.2″) beam and poor recovery of large angular scale emission. This image highlights the presence of protostellar cores on the left edge of the bubble and along a filament just south of the central source. (*Right*): A robust +2.0 image with a larger (0.4″) beam and better recovery of large angular scales. The contours show radio continuum (14.5 GHz) emission at 1.5, 3, and 6 mJy/beam. While some of the detected 1.4 mm emission in the south could be free-free emission, the eastern and northern parts of the shell show no emission down to the 50 μJy noise level of the Ku-band map, confirming that they consist only of dust emission.

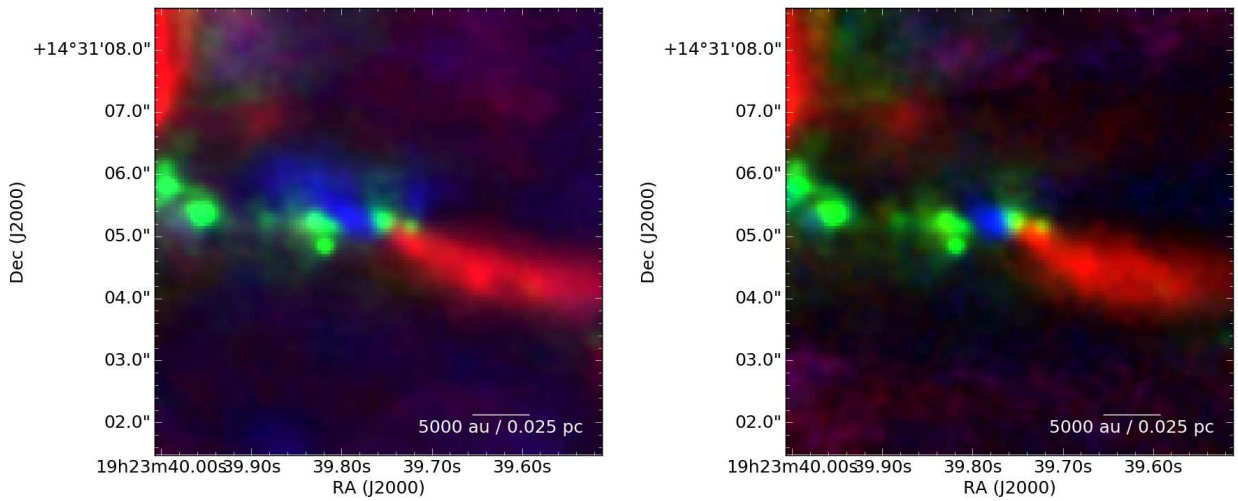

(a) (b)

Fig. B.1. Outflows shown in red and blue for (a) CO 2-1 and (b) SO $6_5 - 5_4$ with continuum in green. This symmetric molecular outflow forms the base of the Lacy et al. (2007) ionized outflow detected further to the east. The continuum source is offset from the line joining the red and blue outflow lobes.

(Figure B.3). To the southeast, the high-velocity flow lies along a line that is consistent with the extrapolation from the northwest flow, but at lower velocities ($10 < v_{LSR} < 45$ km s^{-1}), it jogs toward a more north-south direction (Figure B.4). In the northwest, the redshifted part of this flow ($70 < v_{LSR} < 120$ km s^{-1}) apparently collides with a *blue*shifted flow from another source ($22 < v_{LSR} < 45$ km s^{-1}), suggesting that these outflows intersect, though such a scenario seems implausible given their small volume filling factor.

The extreme velocity and morphology carry a few implications for the accretion process in W51. The sharp symmetric truncation, combined with the extraordinary velocity, suggests that the outflow is freshly carving a cavity in the surrounding dense gas. The observed velocities are high enough that their bow shocks likely dissociated all molecules, so some ionized gas is likely present at the endpoints; this ionized gas has not been detected in radio images because of the nearby 100 mJy HCHII region e2w. The dynamical age of the outflow is $\sim$ 600 years at the peak observed velocity, which is a lower limit on the true age of the outflow.

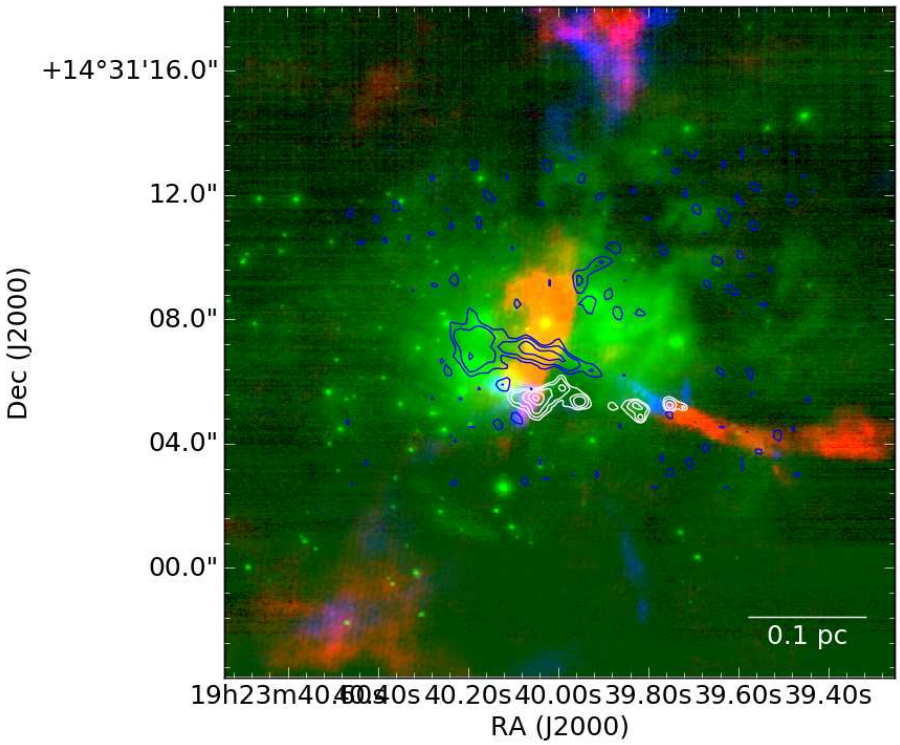

Fig. B.2. Outflows in the W51 IRS2 region. The green emission is NACO K-band continuum (Barbosa et al. 2008), with ALMA 1.4 mm continuum contours in white and H77α contours in blue. The Lacy et al. (2007) jet is prominent in H77α.

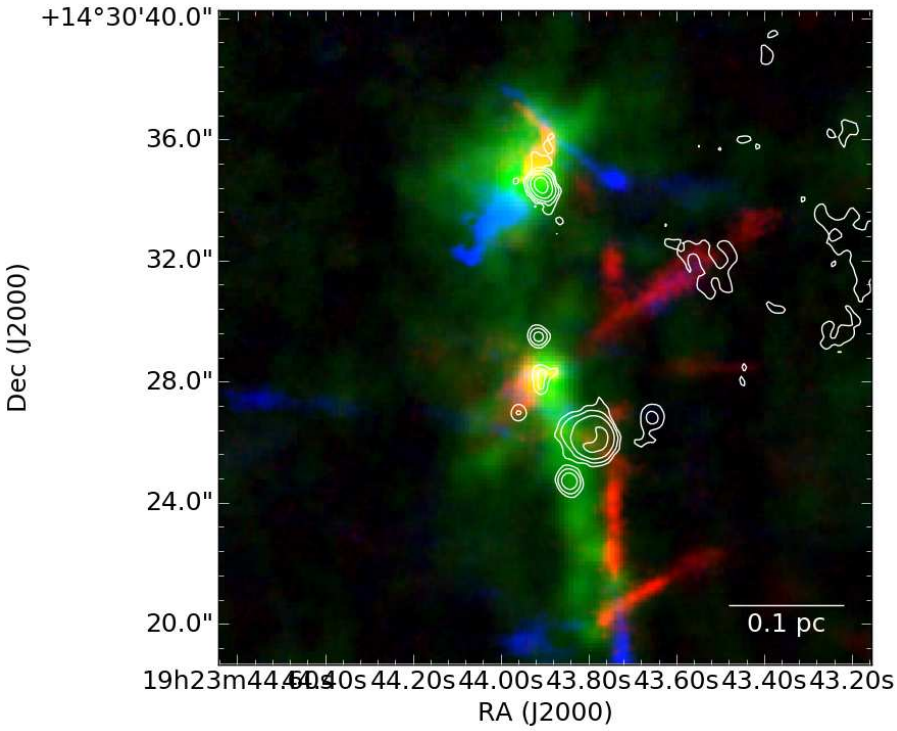

Fig. B.3. Outflows in red and blue overlaid on mm continuum in green with cm continuum contours in white. The northern source is e2, the southern source at the tip of the long continuum filament is e8.

Appendix B.0.4: e8

There are at least four distinct outflows coming from the e8 filament. The e8 core is launching a redshifted outflow to the northwest. A blueshifted outflow is coming from somewhere south of the e8 peak and pointing straight east. While these originate quite near each other, they seem not to have a common source, since the red and blue streams are not parallel (Figures B.3 and B.5). The e8 outflows are too confused and asymmetric for simple interpretation.

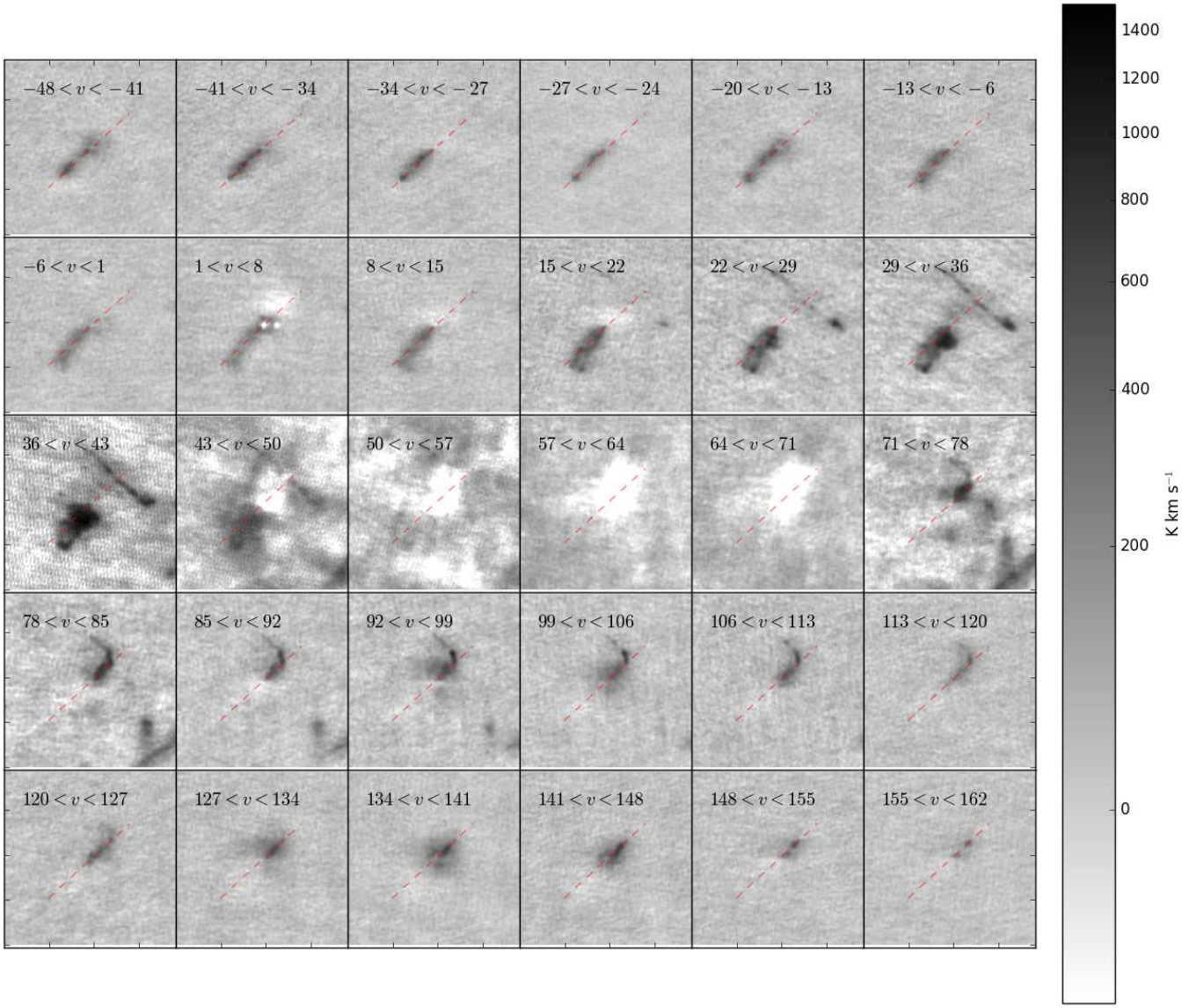

Fig. B.4. Channel maps of the e2e outflow in CO 2-1. The dashed line approximately connects the northwest and southeast extrema of the flow.

Appendix C: Details of the extracted sources

We provide additional information and details about the continuum source extraction, along with complete catalogs, in this Appendix.

Appendix C.1: The spatial distribution of continuum sources

The detected continuum sources are not uniformly distributed across the observed region. The most notable feature in the spatial distribution is their alignment: most continuum sources collect along approximately linear features. This is especially evident in W51 IRS2, where the core density is very high and there is virtually no deviation from the line. The e8 filament is also notably linear, though there area few sources detected just off the filament.

On a larger scale, the e8 filament points toward e2, apparently tracing a slightly longer filamentary structure. With some imagination, this might be extended along the entire northeast ridge to eventually connect in a broad half-circle with the IRS2 filament (Figure C.1). This morphology hints at a possible sequential star formation event, where some central bubble has swept gas into these filaments. However, this ring has no counterparts in ionized gas, and there is little reason to expect such circular symmetry from a real cloud, so the star forming circle may be merely a figment.

Whether it is physical or not, there is a notable lack of continuum sources within the circle. There is no lack of molecular gas, however, as both CO and H_2CO emission fill the full field of view.

Appendix C.2: Photometry

We created a catalog of the hand-extracted sources including their peak and mean flux density, their centroid, and their geometric properties. For each source, we further extracted aperture photometry around the centroid in 6 apertures: 0.2, 0.4, 0.6, 0.8, 1.0, and 1.5″. We performed the same aperture photometry on the W51 Ku-band images from Ginsburg et al. (2016b) to estimate the free-free con-

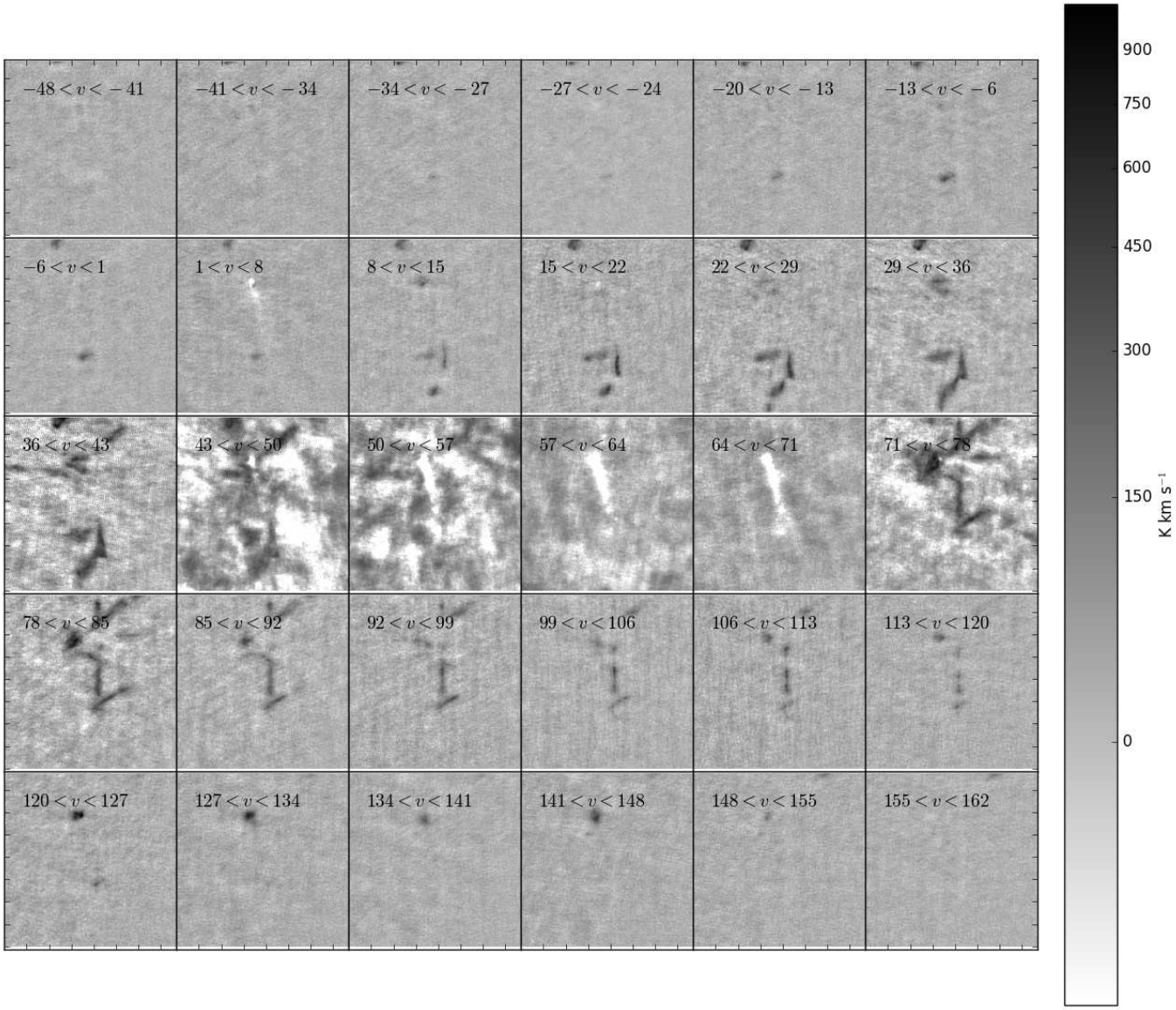

Fig. B.5. Channel maps of the e8 outflow in ^{12}CO 2-1. The outflows here are more erratic, with fewer clearly-connected red and blue lobes.

tribution to the observed flux density measurements. These measurements are reported in Table C.2.

The source flux density distribution is shown in Figure C.2. The most common nearest-neighbor separation between cataloged sources is $\sim 0.3''$, which implies that the larger apertures double-count some pixels. The smallest separation is $0.26''$, so the $0.2''$ aperture contains almost only unique pixels. The corresponding masses are shown in Figure C.5 assuming the dust temperature is equal to the source's peak line brightness temperature (Section C.3).

Except where noted below, the hand-selected sources are used for further analysis as they are more reliable.

Appendix C.3: Temperature estimation of the continuum sources

The temperature is a critical ingredient for determining the total mass of each continuum source or region. Since we do not have any means of directly determining the dust temperature, as the SED peak is well into the THz regime and inaccessible with any existing instruments at the requisite resolution, we employ alternative indicators. Above a density $n \gtrsim 10^5 - 10^6$ cm^{-3}, the gas and dust become strongly collisionally coupled, meaning the gas temperature should accurately reflect the dust temperature. Below this density, the two may be decoupled.

The average dust temperature, as estimated from Herschel Hi-Gal SED fits (Molinari et al. 2016; Wang et al. 2015), is 38 K when including the 70 μm data or 26 K when excluding it. This average is obtained over a $\sim 45''$ (~ 1 pc) beam and therefore is likely to be strongly biased toward the hottest dust in the HII regions. Despite these uncertainties, this bulk measurement provides us with a reasonable range to assume for the uncoupled, low-density dust, which (weakly) dominates the mass (see Section 3.2).

One constraint on the dust temperature we can employ is the absolute surface brightness. For some regions, especially the e8 filament and the hot cores, the surface brightness is substantially brighter than is possible for a beam-filling, optically thick blackbody at 20 K, providing

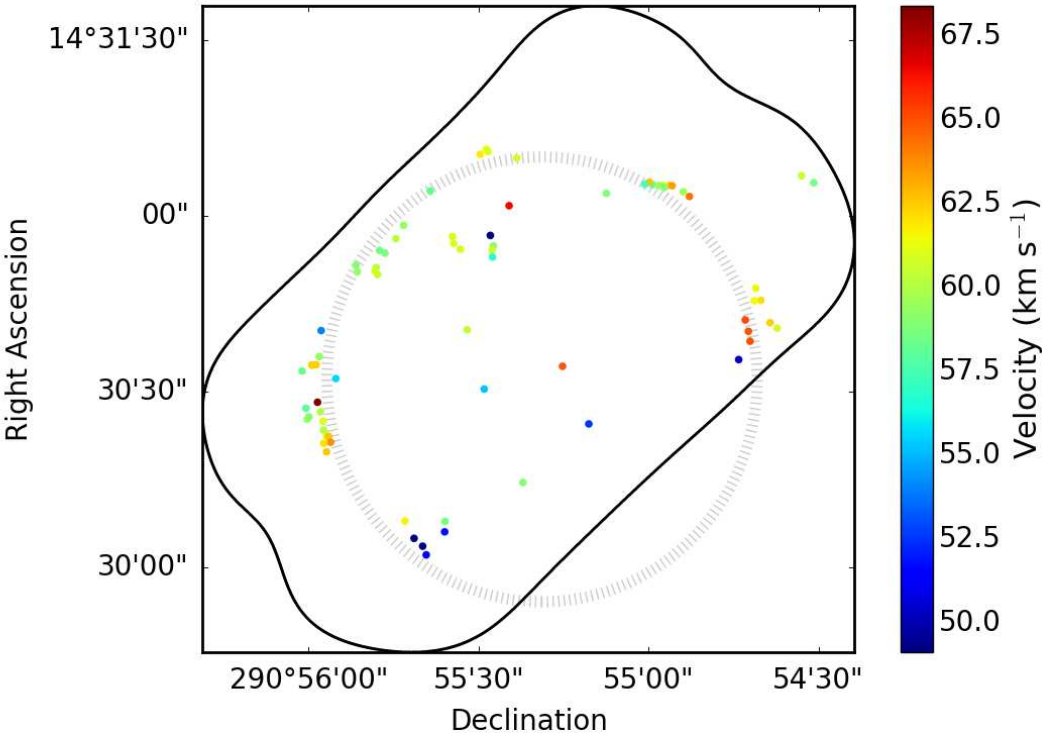

Fig. C.1. The spatial distribution of the hand-identified core sample. The black outer contour shows the observed field of view. The dashed circle shows a hypothetical ring of star formation.

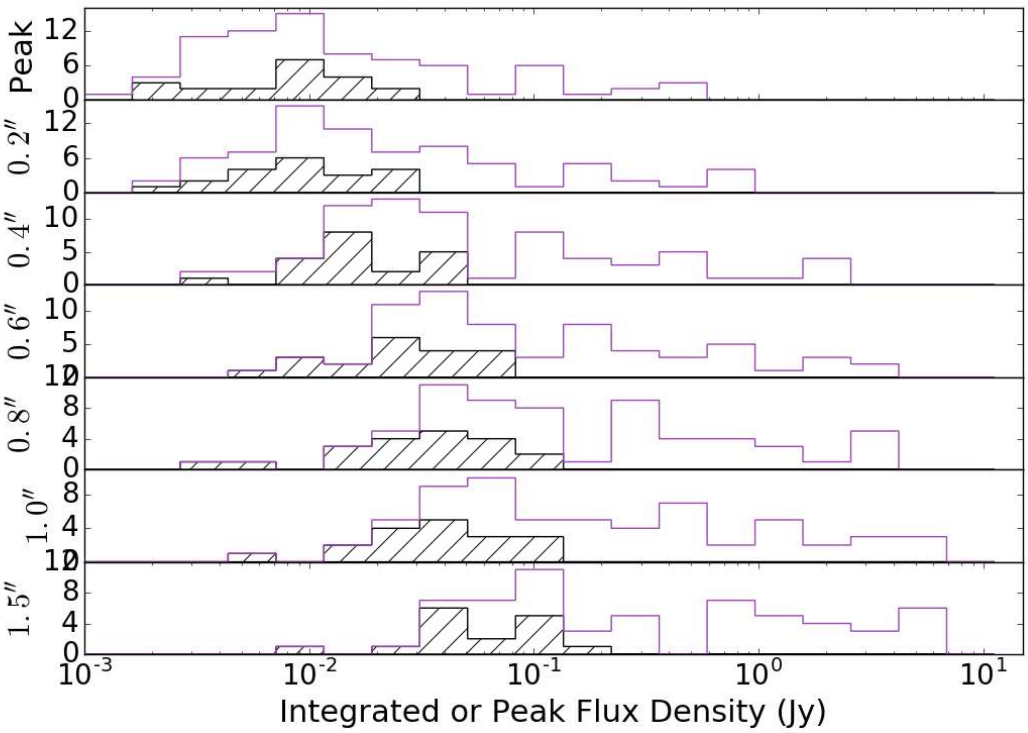

Fig. C.2. Histograms of the core flux densities measured with circular apertures centered on the hand-extracted core positions. The aperture size is listed in the y-axis label. For the top plot, labeled 'Peak', this is the peak flux density in Jy/beam. For the rest, it is the integrated flux density in the specified aperture. The unfilled data show all sources and the hashed data are for starless core candidates (Section C.4). See Figure C.5 for the corresponding masses.

Table C.1. Continuum Source IDs and photometry Part 1

Source ID	RA °	Dec °	$S_\nu(0.2'')$	$S_\nu(0.4'')$	$T_{B,max}$ K	M(T_B, 0.2″) $M_\odot$	M(T_B, peak) $M_\odot$	Categories
ALMAmm1	290.9286	14.5022		0.01	11	2.6	2.6	fCc
ALMAmm10	290.9114	14.5132		0.01	5.3	2.6	1	-Cc
ALMAmm11	290.9112	14.5127	0.02	0.04	12	14	12	-Cc
ALMAmm12	290.9115	14.5127	0.01	0.02	11	3.7	11	-C-
ALMAmm13	290.9118	14.5112	0.01	0.01	11	5	8.6	-Cc
ALMAmm14	290.9107	14.5116	0.07	0.14	36	23	23	–c
ALMAmm15	290.9104	14.5114	0.01	0.03	35	4.9	8.1	–c
ALMAmm16	290.9092	14.5186	0.02	0.04	5.6	16	32	-Cc
ALMAmm17	290.9259	14.5151	0.01	0.03	12	11	5	fCc
ALMAmm18	290.9262	14.5154	0.01	0.03	5.6	11	4.1	-Cc
ALMAmm19	290.9263	14.5157		0.01	21	3.2	1.4	—
ALMAmm2	290.9266	14.5022		0.01	4	3	12	fCc
ALMAmm20	290.9235	14.5172	0.01	0.02	6.6	5.7	4	-C-
ALMAmm21	290.9249	14.5196	0.01	0.01	nan	6.3	31	–c
ALMAmm22	290.9246	14.5198	0.01	0.02	nan	6.1	18	—
ALMAmm23	290.9187	14.5178	0.02	0.07	26	11	5.2	—
ALMAmm24	290.9165	14.5182	0.29	0.6	72	46	32	-Hc
ALMAmm25	290.9255	14.5113	0.02	0.04	3.8	13	6	fCc
ALMAmm26	290.9296	14.5149	0.01	0.03	8.9	9.5	14	-Cc
ALMAmm27	290.9290	14.5156	0.01	0.03	5	7.2	8.2	fC-
ALMAmm28	290.9320	14.5090	0.02	0.03	19	11	6.5	-Cc
ALMAmm29	290.9247	14.5085	0.01	0.02	nan	6.4	11	f-c
ALMAmm3	290.9267	14.5017		0.01	nan	3	2.9	f–
ALMAmm30	290.9298	14.5150	0.01	0.02	4.3	5.9	2	fCc
ALMAmm31	290.9156	14.5181	0.17	0.36	46	43	16	–c
ALMAmm32	290.9155	14.5181	0.09	0.23	94	1	13	-H-
ALMAmm33	290.9160	14.5181	0.19	0.51	48	48	18	—
ALMAmm34	290.9162	14.5181	0.08	0.24	9	1	1	-H-
ALMAmm35	290.9166	14.5183	0.2	0.58	34	76	18	—
ALMAmm36	290.9147	14.5176	0.02	0.05	11	16	6.5	-Cc
ALMAmm37	290.9243	14.5152	0.02	0.04	34	6.4	3.1	–c
ALMAmm38	290.9209	14.5095			2	1.7	15	-Cc
ALMAmm39	290.9245	14.5197	0.01	0.02	3.4	5.5	25	-C-
ALMAmm4	290.9276	14.5006	0.01	0.02	11	5.4	6.1	-Cc
ALMAmm40	290.9231	14.5194	0.01	0.02	9.2	5.3	5.5	-Cc

a lower limit on the dust temperature ranging from 20 K (35 mJy/beam) to $\sim$ 300 K (0.5 Jy/beam). Toward most of this emission, optically-thick free-free emission can be strongly ruled out as the driving mechanism using existing data that limits the free-free contribution to be $< 50\%$ if it is optically thick, and negligible ($<< 1\%$) if it is optically thin at radio wavelengths (Ginsburg et al. 2016a; Goddi et al. 2016).

To gain a more detailed measurement of the dust temperature in regions where it is likely to be coupled to the gas, we use the peak brightness temperature $T_{B,max}$ of spectral lines along the line of sight. If the observed molecule is in local thermal equilibrium, as is expected if the density is high enough to be collisionally coupled to the dust, and it is optically thick, the brightness temperature provides an approximate measurement of the local temperature near the $\tau = 1$ surface. If any of these assumptions do not hold, $T_{B,max}$ will set a lower limit on the true gas temperature. Only two mechanisms can push $T_{B,max} > T_{dust}$: nonthermal (maser) emission or a dust-emitting region that has a smaller beam filling factor than the gas-emitting region.

One potential problem with this approach is if the gas becomes optically thick before probing most of the dust. Some transitions of more abundant molecules, e.g., CO and H_2CO, are likely to be affected by this issue. However, many of the molecules included in the observations have lower abundances and are likely to be optically thin along most of the line of sight.

Some sources have no detected line emission aside from the molecular cloud species CO and H_2CO. The minimum density requirement imposed by a continuum detection at our limit of 1.6 mJy is $n > 10^{7.5}$ cm^{-3} for a spherical source. At such high density, it is unlikely that the species are undetected because they are subthermally excited. More likely, the line-nondetection sources have an underyling emission source that is very compact, optically thick, and/or cold.

Figure C.3 shows the distribution of peak line brightnesses for the continuum sources. The spectra used to determine this brightness are the spectra obtained from the brightest continuum pixel within the source aperture. To obtain the peak line brightness, we fit Gaussian profiles to each identified line listed in Tables 2-5, rejecting those with poor fits. The line brightnesses reported in the figure are the sum of the continuum-subtracted peak line brightness and the continuum brightness (i.e., they are the raw observed peak brightness). Excepting CO and H_2CO, which

Table C.2. Continuum Source IDs and photometry Part 2

Source ID	RA °	Dec °	$S_\nu(0.2'')$	$S_\nu(0.4'')$	$T_{B,max}$ K	M(T_B, 0.2″) $M_\odot$	M(T_B, peak) $M_\odot$	Categories
ALMAmm41	290.9327	14.5112	0.02	0.03	3	8.6	13	–c
ALMAmm43	290.9150	14.5178	0.02	0.05	17	14	4.8	fC-
ALMAmm44	290.9086	14.5182	0.01	0.02	5.7	6	28	-Cc
ALMAmm45	290.9115	14.5187	0.01	0.02	4.4	5.2	1.8	-C-
ALMAmm46	290.9243	14.5147	0.01	0.04	24	8.5	3	—
ALMAmm47	290.9274	14.5179	0.01	0.01	4.9	4.5	9.2	-Cc
ALMAmm48	290.9287	14.5162	0.01	0.02	8.1	6.7	13	-Cc
ALMAmm49	290.9300	14.5142	0.01	0.05	21	9.8	7.6	—
ALMAmm5	290.9277	14.5010	0.01	0.02	5.9	7.3	8.8	-Cc
ALMAmm50	290.9301	14.5141	0.02	0.05	14	14	6.3	-C-
ALMAmm51	290.9300	14.5139	0.02	0.05	16	13	2.7	-C-
ALMAmm52	290.9117	14.5107		0.01	7.9	3.5	1	-Cc
ALMAmm53	290.9119	14.5117	0.01	0.02	13	5.7	5.6	-Cc
ALMAmm54	290.9122	14.5099	0.01	0.01	2.5	3.6	9.7	-Cc
ALMAmm55	290.9309	14.5140	0.01	0.03	4.5	7.7	6.5	-C-
ALMAmm56	290.9310	14.5143	0.01	0.03	5.3	6.4	5.4	-C-
ALMAmm57	290.9239	14.5147	0.01	0.01	2	4	1.2	fCc
ALMAmm6	290.9282	14.5014		0.01	3.8	2	1.1	fC-
ALMAmm7	290.9196	14.5068		0.01	1.4	2.5	7.1	-Cc
ALMAmm9	290.9228	14.5041	0.02	0.05	5.8	15	9	-Cc
d2	290.9159	14.5180	0.16	0.43	99	18	15	-H-
e1mm1	290.9327	14.5074	0.16	0.42	23	95	31	—
e2e	290.9332	14.5096	0.69	1.9	84	94	61	-H-
e2e peak	290.9332	14.5096	0.74	1.8	1	8	68	-Hc
e2nw	290.9328	14.5100	0.22	0.51	4	69	33	–c
e2se	290.9337	14.5093	0.04	0.1	93	4.4	7.3	-H-
e2w	290.9330	14.5096	0.54	1.2	85	72	6	fHc
e3mm1	290.9326	14.5069	0.05	0.18	23	29	9.4	—
e5	290.9244	14.5157	0.03	0.03	nan	18	34	F-c
e8mm	290.9329	14.5078	0.68	1.7	18	43	16	-H-
eEmm1	290.9334	14.5070	0.04	0.1	39	12	7	—
eEmm2	290.9333	14.5071	0.04	0.1	22	24	6.5	—
eEmm3	290.9335	14.5075	0.04	0.1	22	27	8.1	–c
eSmm1	290.9326	14.5065	0.07	0.18	34	26	2	—
eSmm2	290.9325	14.5062	0.07	0.17	29	31	23	–c
eSmm2a	290.9323	14.5062	0.05	0.13	24	28	18	—
eSmm3	290.9323	14.5059	0.05	0.1	29	23	16	–c
eSmm4	290.9326	14.5059	0.04	0.1	27	17	1	—
eSmm6	290.9325	14.5055	0.05	0.11	23	29	15	–c
north	290.9169	14.5182	0.72	1.7	69	12	59	-Hc

The Categories column consists of three letter codes as described in Section C.4.In column 1, `F` indicates a free-free dominated source,`f` indicates significant free-free contribution,and - means there is no detected cm continuum.In column 2, the peak brightness temperature is used toclassify the temperature category.`H` is 'hot' ($T > 50$ K), `C` is 'cold' ($T < 20$ K), and - is indeterminate (either $20 < T < 50$K or no measurement)In column 3, `c` indicates compact sources, and - indicates a diffuse source.

are excluded from the plot, CH_3OH is the brightest line toward most sources.

We use these peak line brightness temperatures to compute the 'corrected' masses of the continuum sources. For sources with $T_{B,max} < 20$ K, we assume $T_{dust} = 20$ K to avoid producing unreasonably high masses; in such sources the lines are likely to be optically thin and/or subthermally excited. The correction is illustrated in Figure C.4.

This section has provided some simple temperature estimates across all of the detected continuum sources. In Section 3.4, we examine the thermal structure of the hot cores in more detail.

Appendix C.4: The nature of the continuum sources

Millimeter continuum sources in star-forming regions are usually assumed to be either protostars or starless cores. However, in this high-mass star-forming region, we have to consider both those possibilities and potential free-free sources or high-luminosity main-sequence stars embedded in dust.

We fit each of up to ~ 50 lines (see Tables 2-5) with Gaussian profiles to attempt to determine the relative line strengths toward each source. Most sources were detected in at least $\sim 5-10$ lines, though some of these are associated with interstellar rather than circumstellar material, i.e., H_2CO, CO, ^{13}CS. For sources with detections in non-

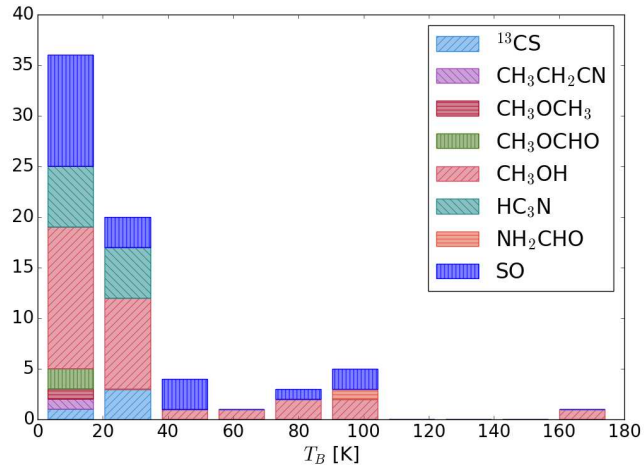

Fig. C.3. Histogram of the brightest line toward each continuum source. The bars are colored by the molecular species associated with the brightest line that is not associated with extended molecular cloud emission, i.e., CO and its isotopologues and H_2CO are excluded.

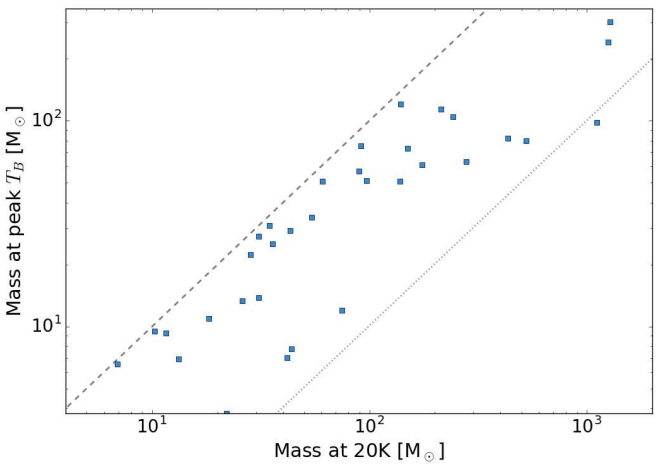

Fig. C.4. The mass computed assuming the dust temperature is the peak brightness temperature vs. that computed assuming $T_{dust} = 20$ K for the aperture extracted continuum sources. The dashed line shows $M(T_{B,max}) = M(20\mathrm{K})$ and the dashed line shows $M(T_{B,max}) = 0.1M(20\mathrm{K})$

interstellar lines, we used the peak brightness temperature of the line as an estimated lower limit on the core temperature.

In the continuum, we measured a 'concentration parameter', which is the ratio of the flux density in a 0.2″ aperture to that in a 0.2″-0.4″ annulus divided by three to account for the annulus' larger area. A uniform source with $r > 0.4''$ source would have a concentration $C = 1$ by this definition, while an unresolved point source would have a Gaussian profile resulting in $C = 14$. Only one source approaches this extreme, the HII region e5, while the rest have $C \leq 7$. We set the threshold for a 'concentrated' source to be $C > 2$, which is arbitrary, but does a reasonable job of distinguishing the sources with a clear central concentration from those that have none.

Main sequence OB stars and their illuminated ionized nebulae are in principle easily identified by their free-free emission. Starless cores, protostellar cores, and their variants are more difficult to identify, so we used a combination of temperature and concentration parameter to classify them.

We classified each of the 75 hand-selected sources on the following parameters:

1. Free-free dominated sources ($S_{15GHz} > 0.5S_{226GHz}$) are H II regions
2. Free-free contaminated sources ($S_{15GHz} > 0.1S_{226GHz}$) are likely to be dust-dominated but with H II region contamination; these are either dusty sources superposed on or embedded in a large H II region or they are compact, dusty H II regions
3. Starless core candidates were identified as those with cold peak brightness temperatures $T_B < 20$ K and with a high concentration parameter ($C > 2$)
4. Hot core candidates are those with peak $T_B > 50$ K and $C > 2$
5. Extended cold core and hot core candidates are those with $T_B < 20$ and $T_B > 50$ K and $C < 2$
6. The remaining sources with $S_{15GHz} < 0.1S_{226GHz}$ and $50 > T_B > 20$ K were classed as uncertain compact ($C > 2$) or uncertain extended ($C < 2$)

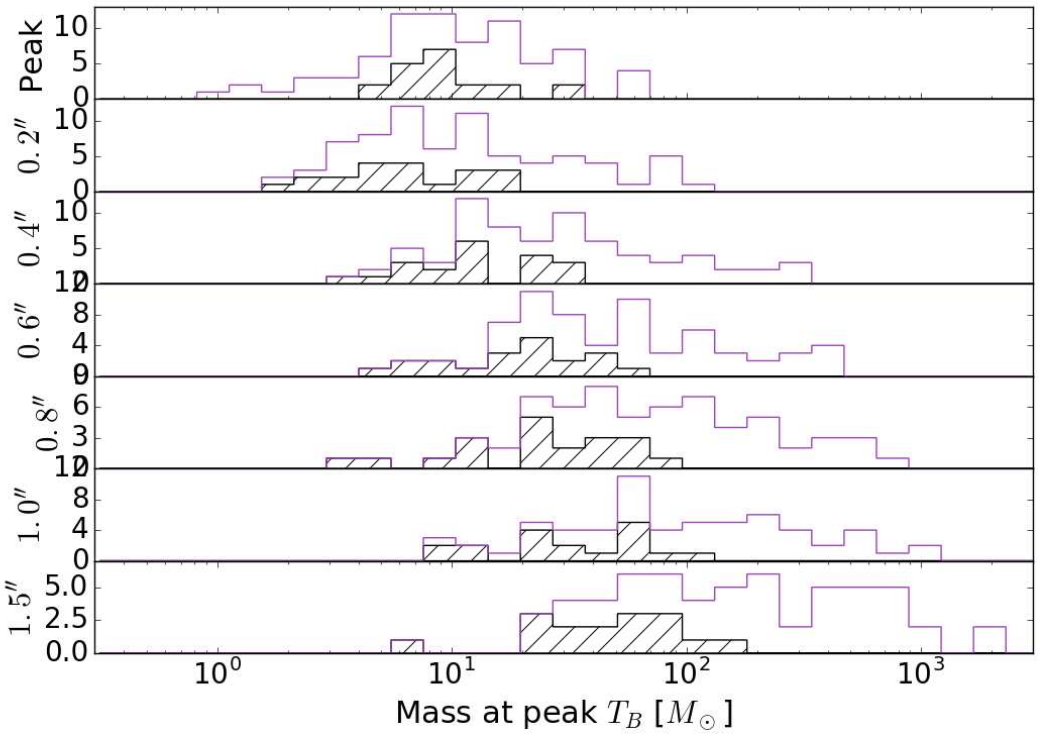

Fig. C.5. Histograms of the core masses computed from the flux density measurements shown in Figure C.2 using the peak brightness temperature toward the center of that source as the dust temperature. The aperture size is listed in the y-axis label. For the top plot, labeled 'Peak', the mass is computed from peak flux density in Jy/beam. For the rest, it is the integrated flux density in the specified aperture in Jy. The unfilled data show all sources and the hashed data are for starless core candidates (Section C.4).

These classifications are set in the 'Categories' column of Table C.2. They serve as a broad guideline for further analysis.